New insights into the mechanism of ultrasonic atomization for the production of metal powders in additive manufacturing

Abhinav Priyadarshi [a,*], Shazamin Bin Shahrani [a], Tomasz Choma [b,c], Lukasz Zrodowski [b,c], Ling Qin [d], Chu Lun Alex Leung [e,f], Samuel J. Clark [g], Kamel Fezzaa [g], Jiawei Mi [h], Peter D. Lee [e,f], Dmitry Eskin [i], Iakovos Tzanakis [a,j]

[a] Faculty of Technology, Design and Environment, Oxford Brookes University, Oxford, UK
[b] Faculty of Materials Science and Engineering, Warsaw University of Technology, Woloska 141 St., Warsaw 02-507, Poland
[c] Amazemet Sp. z o.o. [Ltd]. Al., Warsaw, Poland
[d] Center of Innovation for Flow Through Porous Media, Department of Petroleum Engineering, University of Wyoming, Laramie, WY, USA
[e] Department of Mechanical Engineering, University College London, London, UK
[f] Research Complex at Harwell, Harwell Campus, Oxfordshire, UK
[g] Advanced Photon Source, Argonne National Laboratory, Argonne, IL 60439, USA
[h] School of Engineering, University of Hull, Hull, East Yorkshire, UK
[i] Brunel Centre for Advance Solidification Technology (BCAST), Brunel University London, Uxbridge, UK
[j] Department of Materials, University of Oxford, Oxford, UK

ARTICLE INFO

ABSTRACT

Ultrasonic atomization is one of the promising technologies for producing metal powders for additive manufacturing, where precise control of particle size and morphology is essential. In this study, we coupled an ultrasonic transducer with a carbon fiber plate and atomized liquid droplets and films under different vibration amplitudes. Water, glycerol, and pure aluminum melt were used to study the atomization mechanism and the resulting droplet/powder characteristics, respectively. High-speed optical and ultrafast synchrotron X-ray imaging were used to study *in situ* the ultrasonic atomization dynamics, including pulsation and clustering of cavities inside the liquid layer/films, development of capillary waves, and formation of liquid droplets. For the first time, we observed and captured the occurrence of cavitation during the atomization of resting drops, films and impact droplets. The inertial cavitation events interfered with the capillary waves across the interphase boundary, puncturing and breaking the boundary to produce atomized mist. The *in situ* observation revealed the intricate dynamics of ultrasonic atomization and underscored the pivotal role of cavitation events throughout the entire atomization process. We also conducted experiments on ultrasonic atomization of liquid aluminum, producing particles of perfectly spherical shape. The particle size tended to decrease with reduced vibration amplitude Our work has demonstrated the important processing strategies on how to tailor the particle size while ensuring consistent particle shape and morphology, which is the key processing capability for producing high quality powders for additive manufacturing applications.

1. Introduction

The transformative potential of additive manufacturing (AM) technologies is immense, offering advancements in reduced-waste, complex net-shaped product development across diverse sectors such as aerospace, automotive, medicine, and construction. However, achieving superior material properties in AM products depends on the selection of the material feedstock, e.g. wire, tape, or metal powders [1]. Metal powders play a crucial role in precision AM, and their property and quality profoundly impact the process performance as well as integrity and soundness of the final product [2–4]. Traditional methods, for example, spraying and gas/water atomization are commonly employed for metal powder production in AM processes [5]. However, these methods often suffer from reliability and productivity issues due to inconsistencies in powder properties, resulting in uneven energy absorption and rheological behavior during AM. Consequently, defects such as

closed porosity, keyholes and inconsistent material properties (such as grain texture, uneven composition, or phase distribution within the material) arise, directly influencing the mechanical and functional characteristics of the printed components. Particle size distribution, shape, and surface properties are critical factors in controlling the overall quality of AM components [4]. Hence, it becomes imperative to obtain metal powders that are fine, uniform, spherical, and equally sized for AM and powder metallurgy applications. This requires exploring alternative approaches to produce such powders.

One potential candidate to overcome the aforementioned processing barriers is the ultrasound-assisted melt atomization process [6–9]. This innovative process utilizes ultrasonic vibration to propel tiny droplets from a liquid layer [10,11] and demonstrates outstanding potential in producing high quality powders for AM. Different to the gas-atomization methodologies which is reliant on forceful gas purging through orifices, ultrasonic atomization instead is driven by acoustic waves, triggering the fragmentation of molten metal into fine droplets that promptly solidify upon expulsion from the vibrant surface.

Ultrasound has been employed to produce a diverse range of micro-/nano-sized powders, encompassing lightweight materials, i.e., Al-based [7] and Mg-based alloys [12], and high melting point alloys such as stainless steel [13] and Ti-based alloys [14]. The ultrasonic atomization of low melting point alloys such as lead, tin, and zinc has shown promising results in high yield, uniform, and spherical particles, offering a degree of control over the final particle size distribution by varying the operating frequency [6,9].

The AM of Al-based alloys has garnered substantial attention due to their exceptional specific strength, lightness, stiffness, and machinability. However, the continuous ultrasonic atomization of Al melts needs sufficient ultrasonic vibration amplitude owing to its low density and rapid oxidation of Al droplets when exposed to air and moisture. Innovative strategies have been proposed, including ultrasonic-assisted atomization of a molten salt-Al system [7], achieving the formation of metal microspheres with a minimum diameter close to 15 μm.

Despite significant efforts made in studying the intricate mechanisms of ultrasonic atomization, the atomization mechanism or hypothesis are still under intensive debating [10,11,15–20] with three main theories. The first theory delves into the emergence of capillary (Faraday) wave ripples/patterns that form at the interface between the free liquid surface/film and the surrounding air, triggered by the vibrating transducer [21]. Faraday ripples, also known as Faraday waves, are standing wave patterns that occur on the surface of a fluid subjected to vertical vibrations. These ripples (structured pattern) emerge due to the interplay between gravity, surface tension, and the periodic oscillations induced by the vibrating surface. Atomization occurs when these capillary (Faraday) wave patterns reach a critical amplitude, leading to instable wave patterns that are further fragmented into an array of jets, thus creating droplets [10,11,18,19,22–25]. The second theory considers cavitation as the catalyst for atomization, whereby the implosions of bubbles within the liquid rupture the liquid-air interface, producing the droplets [15,18,26,27]. Under ultrasonic influence, cavitation occurs when localized pressure in a liquid drop below its vapor pressure, resulting in the formation and collapse of air/gas cavities. This phenomenon is contingent upon surpassing a critical ultrasound amplitude, known as the Blake threshold. The presence of a surface is also essential for facilitating heterogeneous nucleation of air/gas cavities, contributing to enhanced cavitation activity. This theory, however, relies upon the atomizer and the frequency employed (usually with frequencies and transducer power rating greater than 100 kHz and 100 W, respectively). The third theory, known as the conjunction theory or the cavitation-wave theory, states that the periodic hydraulic shock waves (SWs) arising from the collapse of bubbles lead to the formation of finite amplitude capillary waves, which, in turn, break apart, yielding aerosol droplets [28,29]. Although the presence of cavitation during ultrasonic atomization process has been indirectly verified through sonoluminescence [30], particle image velocimetry [31], dosimetry

measurements using salicylic acid [32] and iodine irradiation [33], direct visualization of cavitation during the ultrasonic atomization process remains elusive in the current body of literature. To the best of our knowledge, the only visual evidence of cavitation-induced atomization was observed in the liquid flow within microchannels coupled with a transducer, rather than atomization on the direct attachment of a horn/plate system [34].

In our work, we tackle this longstanding debate on the mechanisms governing the ultrasonic atomization process. Using high-speed optical and ultrafast X-ray imaging, we provide, for the first time, the direct evidence that ultrasonic atomization emerges from the synergistic interplay of capillary waves and acoustic cavitation, with the latter serving as the driving and dominating force—a paradigm commonly known as the conjunction theory. One of the promising ways to realize the ultrasonic atomization of Al melts is by employing a vibrating plate sonotrode [35,36], which has a larger surface area and is practically applicable as opposed to the more commonly used ultrasonic horn [37]. However, resolving the intricate mechanism of this dynamic process through real-time *in situ* imaging of molten aluminum poses significant challenges, both in terms of feasibility and safety due to high temperatures and reactivity. Here, we used water as a transparent analog as it exhibits properties closely resembling those of liquid aluminum [38]. Glycerol as a liquid medium was also utilized for certain imaging conditions to better resolve the atomization features that were not possible in case of water. Through the utilization of high-speed optical and X-ray imaging, we investigated the atomization mechanism and dynamics of a single water droplet at rest on the vibrating plate, a liquid film, and droplets impacting onto the vibrating plate and ultrasonic horn operating within the frequency range of 20–60 kHz. Direct observation of internal structures and phenomena associated with droplet decomposition provided a clear insight into the process of ultrasonic atomization. This study was then supported by the atomization of liquid aluminum that offered implication and first-time insights of this technology in producing uniform and high-quality aluminum powders.

2. Experimental methodology

2.1. High-speed optical imaging setup

A schematic representation of the experimental setup is shown in Fig. 1. The ultrasonic transducer employed in this study was a UIP500hdT from Hielscher Ultrasonics GmbH, operating at a frequency of 20 kHz. The transducer offered variable displacement amplitudes, ranging from 11.4 μm (20% input power) to 57 μm (100% input power). To facilitate the experimental configuration, a carbon-fiber (CF) plate supplied by Amazemet Ltd., with dimensions: a length (L) of 200 mm, a width (W) of 40 mm, and a thickness (T) of 1 mm, was connected to the waveguiding system of the transducer, in a cantilever setting at the antinode point of the maximum amplitude. The selection of the CF plate as the atomization platform is driven by its exceptional fatigue resistance at elevated temperatures, attributed to its fibrous structure. When compared to refractory metals, the CF plate exhibits prolonged durability in processes involving liquid metals under ultrasonic agitation. Furthermore, its inherent wettable nature with liquid aluminum, especially under ultrasonic agitation, positions the CF plate as an ideal choice for an atomization platform. Detailed explanation pertaining to its operation and construction can be found elsewhere [39]. Table A1 shows the vibration amplitude of horn and plate sonotrode for different input powers and transducer used in this study.

High-speed imaging was conducted using a FASTCAM SA-Z 2100 K (Photron, Japan) camera with the image acquisition rate of 10–50 kHz, which was determined to strike a balance between object tracking and image resolution. Illumination was provided by a combination of a multi-LED flash lamp (GS Vitec) and a high-power light source (Karl Storz Power LED 175) positioned in front of the experimental setup. The camera was equipped with a Navitar 0.5x lens attachment with a 12×
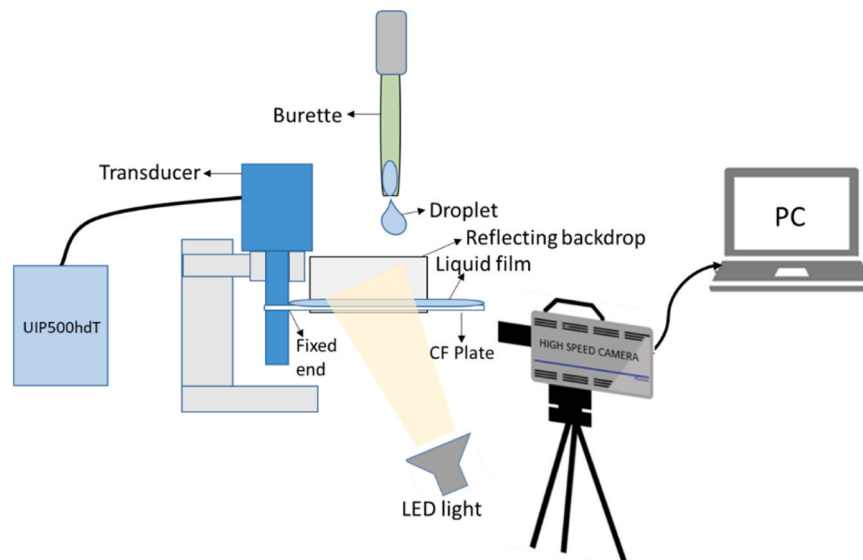
Fig. 1. A schematic, showing the experimental setup for high-speed optical imaging of the ultrasonic atomization process.

zoom combination and a 2.0× adapter, providing a working distance of 165 mm and a maximum depth of field of 6 mm. To optimize image quality, LED lights were directed towards the focal area parallel to the CF plate. A white paper backdrop was used to enhance light reflection from the background, resulting in improved illumination without overexposure.

A contactless custom-made vibrometer (BSUIR) was employed to record the dry CF plate amplitude along its surface. To mitigate any damping effects caused by plate vibrations along its length, particularly away from the sonotrode due to the cantilever effect, the atomization recording area was situated closer to the plate connection with the sonotrode. The plate amplitude was measured along both its length and width in increments of 1 – 2 mm (see Fig. A1 in Appendix), using a translation stage. The measurements revealed a slight decrease in amplitude along the length, while the distance between node and anti-node locations remained constant. In contrast, the amplitude varied across the width of the plate. The distance between consecutive anti-nodes was ca. 12 mm along the length and about 20 mm across the width. The amplitude measurement along the length (Fig. A1a) was conducted across the centreline axis of the plate (see Fig. A1b). At the ultrasonic frequency of 20 kHz, the null-to-peak amplitude of the CF plate ranged from 6 µm to 16 µm at antinodes and from 2 µm to 8 µm at nodes along the flexural length. For simplicity in describing the atomization mechanism, a 20% input power corresponding to an amplitude of 14 ± 1 µm was selected unless explained otherwise. This amplitude was determined to be sufficient for initiating the atomization process. For some cases, glycerol as a liquid was also employed in the experiments. The reason for selecting glycerol as the liquid medium was due to its higher viscosity and larger surface tension, which contributed to decelerating the atomization process. This choice further facilitated detailed observations and analysis of the atomization dynamics due to slower temporal changes compared to water under the same image acquisition conditions. However, atomization of glycerol cannot occur due to very low excitation amplitudes of the vibrating plate transducer. Therefore, instead of using a vibrating plate as for water, a horn transducer with a diameter of 7 mm (UP 200 S Heilschler GmbH) operating at a driving frequency of 24 kHz and having peak-to-peak amplitudes ranging from 35 µm (20% input power) to 175 µm (100% input power) was employed. This choice was deliberate as the horn transducer offered a much higher ultrasonic amplitude, which was roughly three times the amplitude of the plate for the same input power (20%), effectively surpassing the atomization threshold. The buret was used to provide precise control (1–2 ml per second) over the supply of liquid droplets or

flow onto a vibrating plate, ensuring accurate and controlled delivery. To ensure the repeatability of the explained process mechanisms, all experiments were repeated 3–5 times.

2.2. Synchrotron X-ray imaging setup and parameters

The ultrafast synchrotron X-ray imaging of ultrasonic atomization was conducted at the Sector 32-ID-B of the Advanced Photon Source (APS), Argonne National Laboratory. This sector is equipped with an undulator X-ray source designed to deliver 100 ps pulses separated by 153 ns upon synchronizing the pulse from the storage ring with an ultrafast shutter and the beamline camera. The image sequence was recorded using a Shimazdu HyperVision (HPV-X2) camera, coupled with a 10× optical magnification and a fast scintillator crystal (LYSO:Ce) under a 24-bunch mode configuration. To capture a field of view of 1.2 × 0.75 mm for studying the interaction dynamics between the solid-liquid-air interface and the droplet flow during atomization, the imaging process was performed at an acquisition rate of 50 kHz, offering a spatial resolution of 3 µm/pixel. The exposure time for each frame was set at 3000 ns, resulting in a temporal resolution of 20 µs. A white X-ray beam with an average energy of ~24.5 keV was employed in this study. The sample-to-detector (scintillator) distance was set to ~290 mm to optimize the imaging acquisition.

For the liquid atomization, an ultrasonic processor (UP100H) operating at 30 kHz was employed. The setup consisted of a piezoelectric transducer coupled to a titanium sonotrode with a tip diameter of 7 mm. The transducer was positioned in an upright orientation, with the tip pointing upwards. To ensure precise control over the liquid flow rate and enable continuous delivery of small liquid droplets, a programmable syringe pump (SyringeONE NE-1000) was used in the experiments as shown in Fig. 2c. The liquid droplet was dispensed through a 0.32 mm diameter needle onto the tip of the sonotrode. To contain any splashing of the liquid, the sonotrode was enclosed within a plastic tube with dimensions of 66 mm in diameter and 300 mm in height. Within the tube, open slots covered with Kapton tape allowed the X-ray beam to pass through and align with the sonotrode tip. The experimental setup, as described above, is depicted in Fig. 2.

2.3. Liquid aluminum atomization setup

The atomization of pure aluminum melt was carried out using a schematic shown in Fig. 3. Induction heating and a graphite crucible were used to melt the pure Al. The melt was delivered via nozzle of
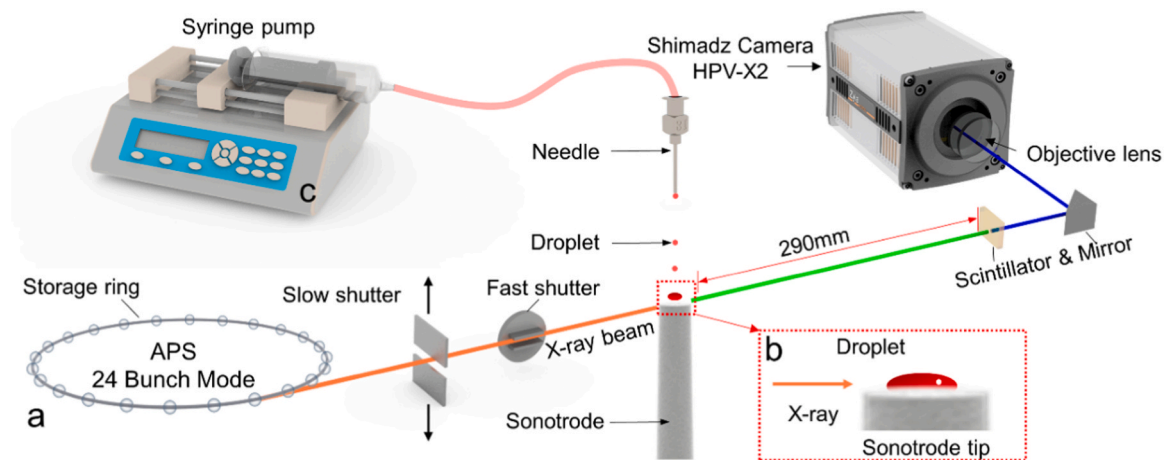
Fig. 2. A schematic, showing the experimental setup for ultrafast synchrotron X-ray imaging of the ultrasonic atomization process at the 32-ID-B of the Advanced Photon Source.
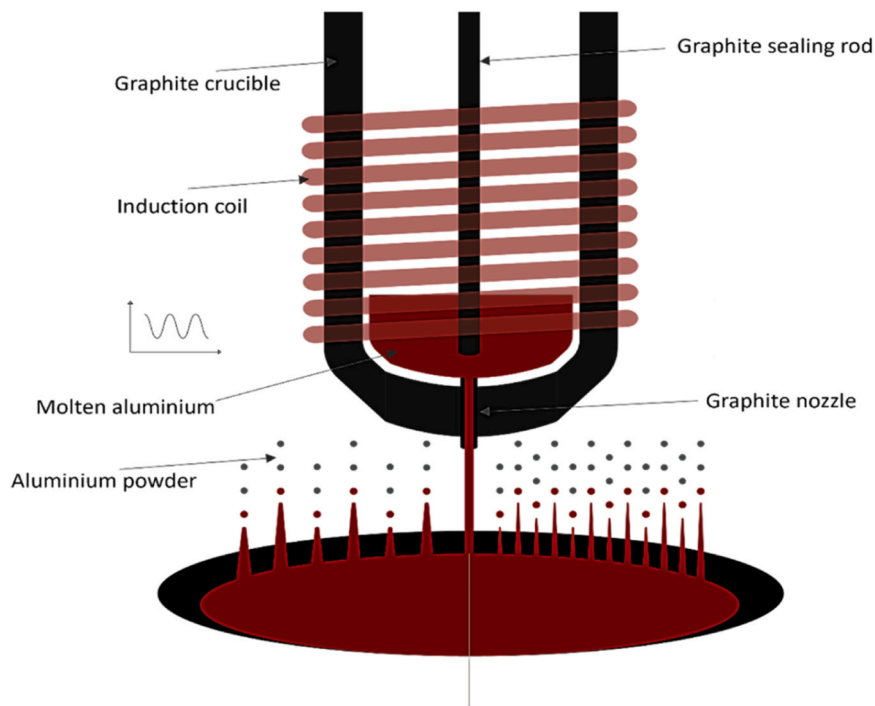

Fig. 3. A schematic, showing ultrasonic atomization setup used for melting and atomizing pure Al melt.

0.5 mm orifice (sealing rod was used to block the melt before pouring). Each process was performed with 250 g of feedstock in the form of granules. The furnace and atomization chamber were purged and filled with argon gas to create an overpressure of 100 mbar and restrict evaporation and oxidation. This created an inert gas atmosphere with an oxygen content below 100 ppm. The material was then melted at a temperature of 800°C, using up to 10 kW of power from the induction furnace. Once the preset temperature was confirmed by a thermocouple placed in the crucible wall, the material was held for an approximate duration of 2 min to ensure temperature uniformity. The molten aluminum was then poured through the nozzle, propelled by a differential pressure of 200 mbar onto the plate sonotrode in the atomization chamber. The sonotrode material was a CF plate and the operating frequency was set at 60 kHz. The atomization started instantly (to the naked eye) and all material was atomized without any interruption. The flow of molten aluminum was regulated by maintaining the appropriate differential pressure and resorting to a turbo pressure of 1.5 bar

whenever signs of nozzle clogging became apparent. The yield from each process consistently exceeded 80%. A scanning electron microscopy (Hitachi SU8000 SEM) was then used to observe the morphology of the powder. The particle size distribution (PSD) of the powders was characterized by using a KAMIKA mini3D laser diffraction analyser. Both volume and number-based PSD were measured, with the output values of D_{10}, D_{50}, and D_{90}, where 10, 50 and 90% of particles were smaller than the indicated size, respectively. The amplitude of the CF plate vibrations was measured using a full-field laser vibrometer PSV-500 (Polytec GmbH) for various input powers.

3. Results and discussion

The first part of this study focuses on the atomization process of a single semi-spherical water drop statically resting on a carbon fiber plate, followed by observations of a stabilized liquid film and finally free fall liquid drop impact. Some examples of atomization of glycerol are

given for a more representative explanation of the atomization process that may not be clearly distinguished with water using optical visualization technique.

In the second part, the results obtained from the synchrotron X-ray imaging experiment are presented and discussed. The real-time collected image data provided direct evidence with new insights for the role of dynamic cavitation in the complex process of ultrasonic atomization that complemented the observations from the optical imaging experiments. All imaging work was conducted under ambient temperature conditions, and the atomization was performed at selected input powers that were well above the cavitation threshold amplitude.

After elucidating the governing mechanisms of ultrasonic atomization in the first two parts, the final part of our study illustrates the practical application of this technique in the production of feedstock powder. The PSD and SEM imaging of atomized aluminum powders obtained for different ultrasonic amplitudes revealed the benefits of using this technology in producing high-quality and uniform feedstock particles for use in AM applications.

3.1. High-speed optical imaging results

3.1.1. Resting drop

Fig. 4a presents the image sequence of the atomization process from the beginning ($t = 0$) to the end ($t = 300$ ms). It shows that the formation of atomized droplets (mist) primarily started around $t \approx 200$ ms with the liquid drop initially spreading along the plate surface and subsequently undergoing atomization. Although the start of atomization can be roughly determined from these images, it is difficult to reveal the micro-features that triggered the atomization process due to the limited spatial resolution. Zooming in on the static droplet with a contact angle of 45 degrees (Fig. 4b), numerous pre-existing cavities (air bubbles in water are common) can be clearly observed at $t = 0$. As the plate transducer was switched on, the individual cavities began to pulsate and cluster

together, forming micro-clouds (encircled in yellow in Fig. 4b2). These ultrasonically excited clouds underwent shape changes, continuous splitting and coalescence, chaotic pulsation with inertial (transient) oscillating behavior possibly leading to the ejection of liquid jets and SWs. However, the emission of liquid jets and SWs could not be visually resolved in this study. At $t = 30.75$ ms, the formation of capillary waves in the form of Faraday ripples with a wavelength of ca. 178 μm occurred on the surface of the liquid drop corresponding to a frequency of ~9.3 kHz. It is interesting to see that from a 20 kHz source, capillary waves (ripples on droplet surface) are formed with almost half the excitation frequency. This wavelength can be influenced by the bubbly cloud size, which can vary depending on the operating conditions of the atomization process. After the development of capillary waves on the surface, the cavitation activity became obscured and visually unidentifiable after $t = 30.75$ ms.

From $t = 30.75$–223.65 ms, the liquid drop exhibited different patterns of capillary waves, with wavelengths increasing to almost 289 μm (~4.5 kHz) at $t = 127.75$ ms and 333 μm (~3.5 kHz) at $t = 133.25$ ms, respectively. Beyond $t = 127.75$ ms, the droplet surface started to lose its stability, resulting in shape fluctuations of its dome. At $t = 176.30$ ms, the stability of the capillary waves started to alter, with an increase in the liquid/air interface contact angle close to 35°, ultimately rupturing followed the formation of liquid droplets (at $t = 223.65$ ms) from specific locations (indicated by red arrows in Fig. 4b7). The instability of the surface profile further increased with more disturbed regions across the interface at $t = 241.95$ ms. Subsequently, the surface of the large drop started to rupture in numerous locations across the interface, resulting in the rapid evolution of small droplets at $t = 256.25$ ms and $t = 270.25$ ms. Finally, at $t = 294$ ms, the entire liquid drop was atomized, as indicated by the flat region over the plate, see details Supplementary Video 1. The stages of capillary wave generation were theorized in ref. [36] and our *in situ* observations have confirmed them.

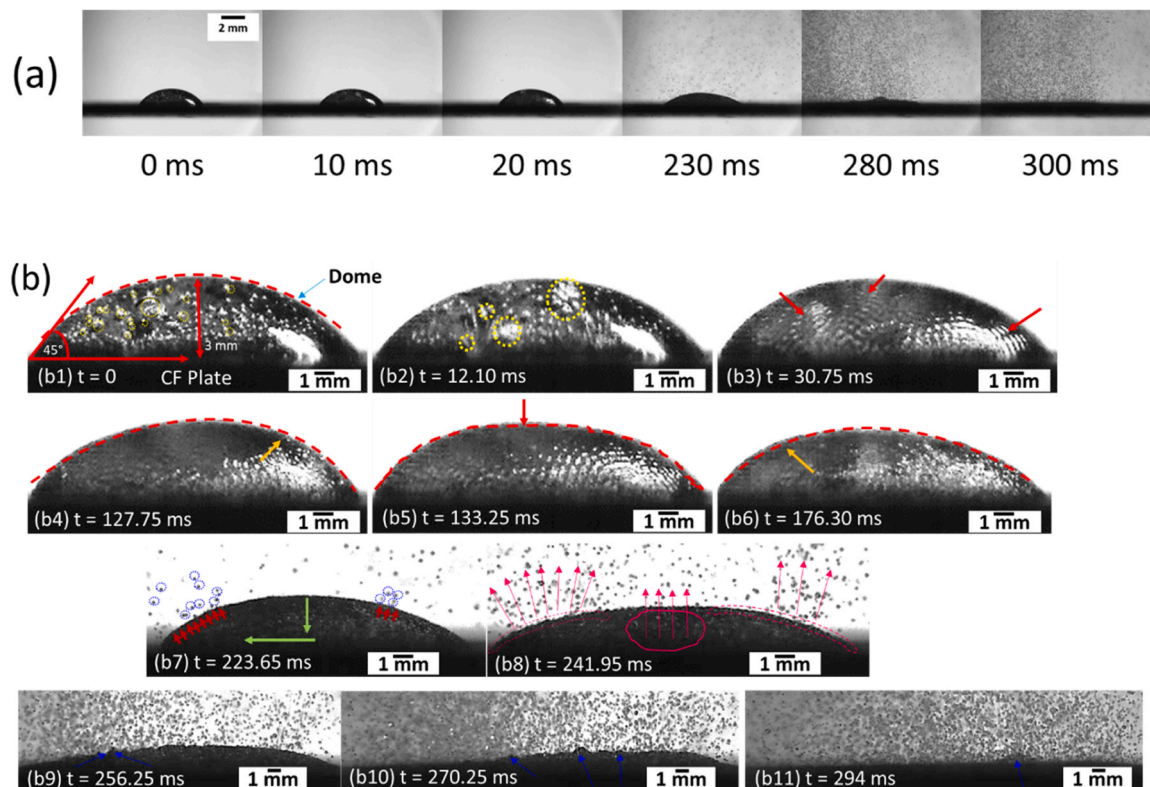Identification of the droplet size and their propulsion speeds based

Fig. 4. High-speed image sequence showing (a) full and (b) time stages of atomization of a single resting water drop on a plate sonotrode captured at an acquisition rate of 20 kHz. See Supplementary Video 1.

on different liquid thickness becomes crucial for the characterization of the generated feedstock during ultrasonic atomization of molten metals such as liquid aluminum and optimization of the overall process. With the help of image processing of real-time high-speed images taken from Supplementary Video 1, we measured the size (diameter) and velocity of the ejected droplets from the atomized cloud for different thicknesses of dome shape. Image processing was performed using in-house developed MATLAB code. The code involved sequential frame processing, encompassing background subtraction, droplet detection through dark pixel counting by inputting necessary parameters such as frame rate, pixel size and intensity threshold. Droplet size was determined by analysing the major axis length of the detected droplets. Velocity calculations involved centroid position comparisons between frames, converting mean distances to m/s. The code yielded statistics on diameters and velocities, providing insights through histograms (Fig. 5).

Supplementary material related to this article can be found online at doi:10.1016/j.addma.2024.104033.

Fig. 5 presents the size and velocity distribution of atomized droplets, which were obtained from liquid water domes with thicknesses of 1.5 mm (Fig. 5a and d), 1 mm (Fig. 5b and e), and 0.5 mm (Fig. 5c and f). The thickness of the dome corresponds to the height of its central portion. With 1.5 mm of dome thickness, the droplet diameter ranged from as low as 37 μm to around 1500 μm with more than 60% of them being below 600 μm. The velocity range was calculated to be 4 – 22 m/s with an average velocity of 11 ± 3 m/s. As the dome thickness dropped to 1 mm, the number of ejected droplets increased with more than 70% of droplets having size lower than 500 μm in diameter and 50% lower than 250μm. This reduction in droplet size is influenced by complex factors such as cavitation, capillary waves, surface area-to-volume ratio, and liquid jet formation. Previous studies have highlighted that larger initial liquid thickness lead to larger droplet formation [40–42]. Thinner liquid films may intensify cavitation, promote capillary wave fragmentation, and increase surface area for nucleation, resulting in finer droplets. Additionally, thinner films may facilitate efficient higher-order harmonic excitation, contributing to smaller droplet formation. The velocity increased by ~36% with average close to 16 m/s and ranged between 11 and 20 m/s. With further decrease of dome thickness to 0.5 mm, the droplet population increased but maximum droplet size reached up to 4000 μm. The large droplet population within the atomized cloud may cause individual droplets to collide with each other in the trajectory following ejection. The average velocity, however, remained unchanged. The high velocities observed in the ejected droplets (around 20 m/s) were attributed to the presence of liquid jets, which are formed by the implosion of cavitation bubbles within the liquid dome. These liquid jets themselves travel at velocities close to 100 m/s or more [43,44]. This observation indirectly supports the argument that the atomization process involves the generation of SWs, which are associated with the rapid and intense collapse of bubbles and the subsequent formation of high-velocity liquid jets. It is important to note here that the underlying mechanisms, particularly cavitation and
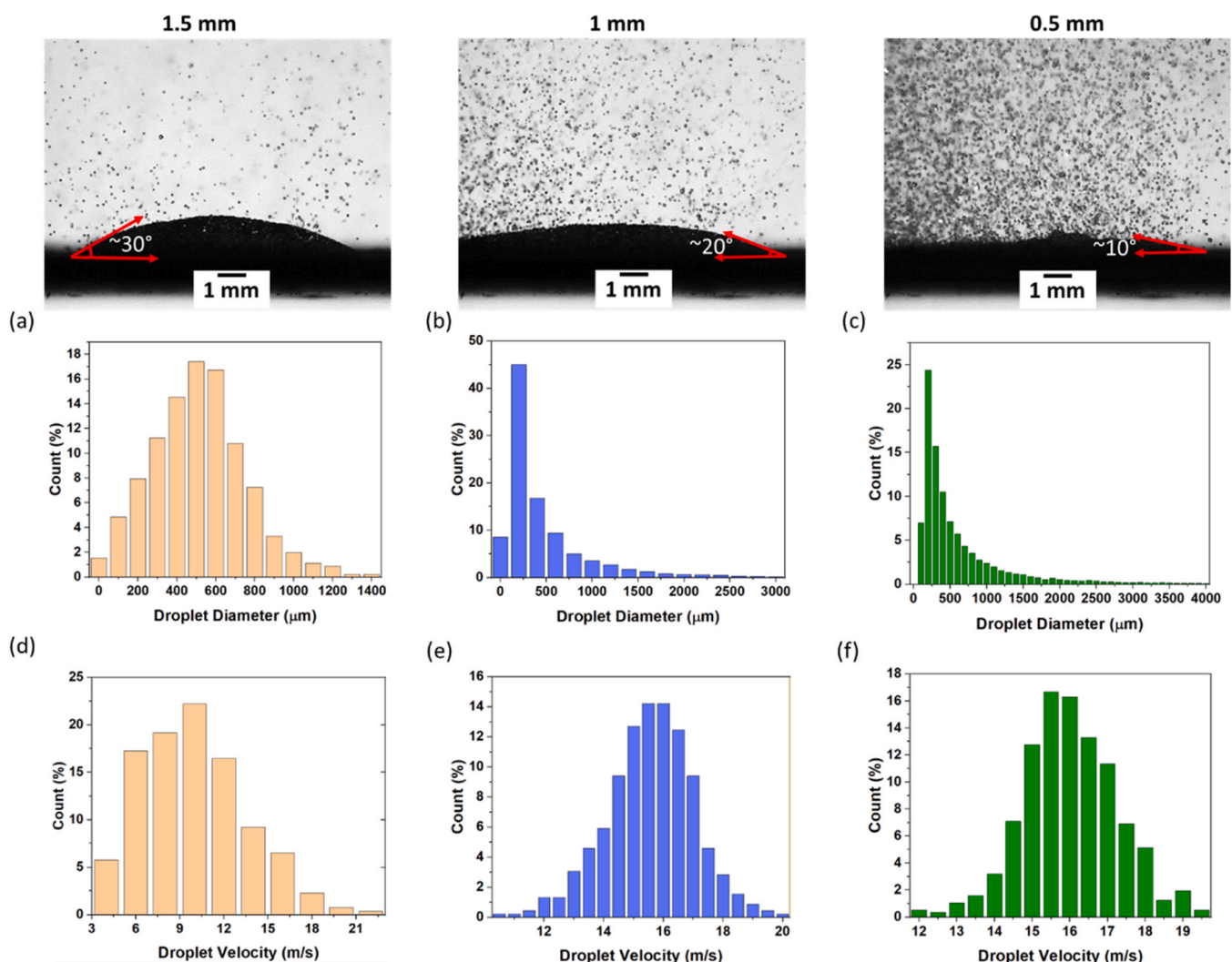

Fig. 5. Histogram showing the distribution of size (a, b and c) and velocity (d, e and f) of ultrasonically atomized droplets obtained for different dome thickness.

capillary wave propagation, dictate the velocity of liquid microjets released upon bubble collapse, that might also influence the ejection velocity of droplets. Cavitation events occurring within the liquid film and near the vibrating surface release a significant amount of energy locally, leading to the ejection of droplets with substantially higher velocities compared to those induced by capillary wave propagation [18]. The interphase surface area also plays a crucial role, as a larger surface area results in increased droplet velocity [10]. Several other studies have highlighted the dependence of droplet velocity on factors such as ultrasonic amplitude and liquid properties [45–47]. Higher amplitude, associated with increased input power, leads to more vigorous cavitation activity and, consequently, higher droplet velocities. Zhang et al. [47] found that the overall velocity of atomized droplets increases sharply with amplitude, which is attributed to the sudden breakup of the liquid surface and subsequent ejection of droplets after absorbing sufficient mechanical energy. However, over time, velocity decreases due to increased air resistance and gravity effects.

In order to gain a better understanding and visualization of cavitation dynamics during the atomization process, another experiment was conducted using glycerol as the liquid medium, effectively slowing down the cavitation evolution.

Fig. 6 presents the frame-by-frame sequence of the atomization process of a glycerol drop on the horn surface (refer to Supplementary Video 2). At $t = 0$, a bubble with a diameter of ca. 300 µm could be seen within the glycerol drop resting on the sonotrode tip. Once the

ultrasound was activated, the bubble began to oscillate and the cavities started forming within the droplet (see red arrows in Fig. 6b). At $t = 2.3$ ms, the small cavitation bubble underwent splitting and coalescing, while the developed cavities vigorously pulsated, eventually forming microbubble clusters. Subsequently, the cavitating clusters became increasingly aggressive (from $t = 3.725$–5 ms), causing distortion of the liquid-air interface in several locations across the periphery (indicated by dashed curved lines). This interface distortion can be considered as the incipient growth of capillary waves, although the capillary waves could not fully establish after the initiation of cavitation, possibly due to the high viscosity of the medium (~1.4 Pa·s compared to 0.001 Pa.s of water at room temperature) unlike observed in the case of water (Fig. 4). The oscillating frequency of the microbubble clusters formed at $t = 2.95$ ms started to decrease from the excitation frequency to about 8 kHz until $t = 5$ ms. This decrease in frequency (subharmonics) has been previously reported to be an indication of hydraulic SWs, thus resulting in non-collapsing deflations [48]. It is important to note here that the development of the capillary wave profile is determined by the interfacial area, and it is affected by the change in the liquid type and its properties, primarily viscosity and surface tension. As the viscosity of the liquid increases, as seen in the case of glycerol, the specific area where the liquid contacts the air (the contact area) decreases. This reduction occurs because the hydraulic SWs lose energy through viscous friction as they are absorbed by the liquid-air interface. Conversely, the decrease in surface tension leads to an increase in the interfacial area
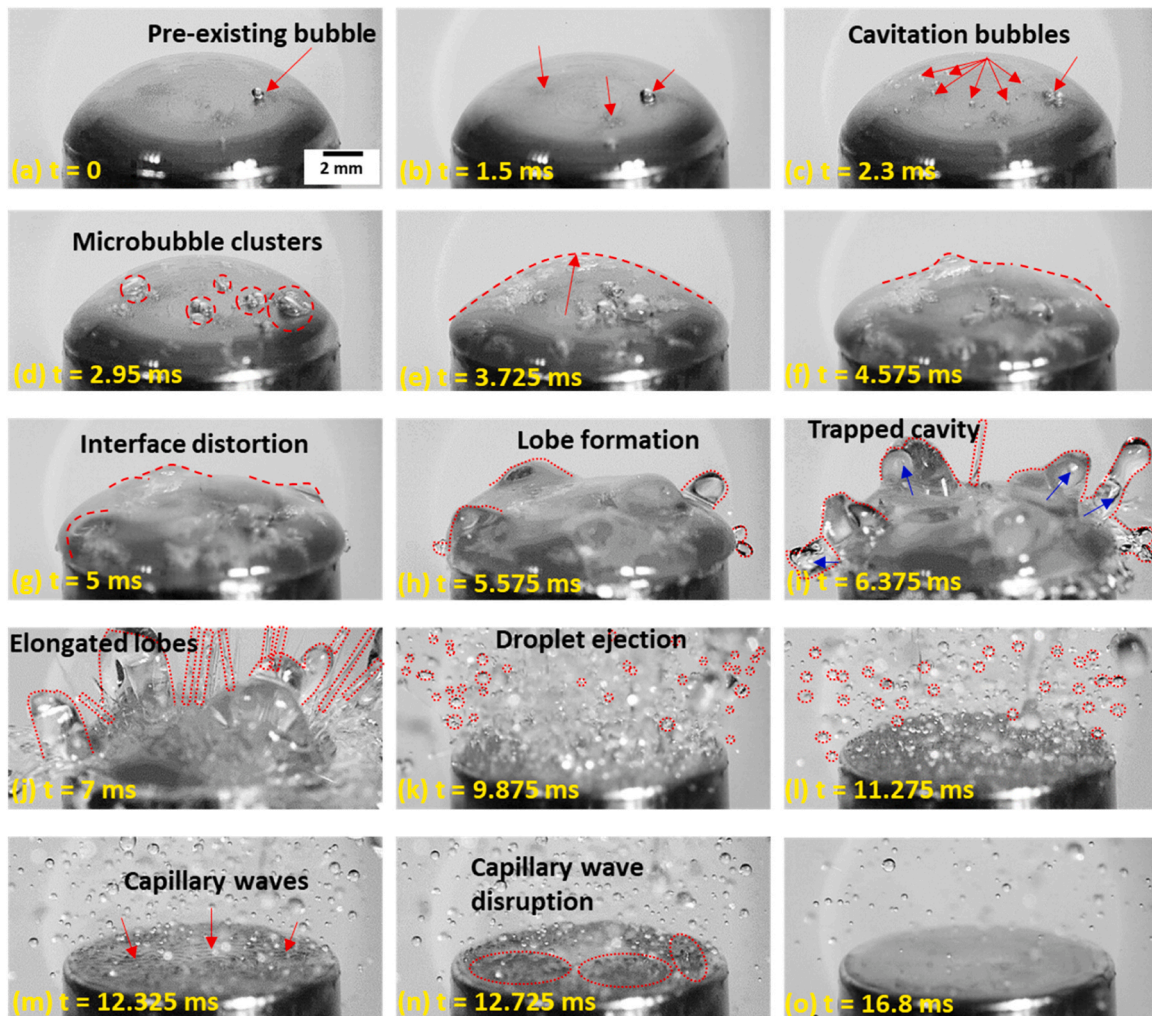

Fig. 6. Series of high-speed images showing full atomization sequence of glycerol droplet resting on an ultrasonic horn captured at an acquisition rate of 40 kHz. See Supplementary Video 2.

since the surface energy is proportional to the interfacial tension [49]. Just after $t = 5$ ms, the distorted interface began to destabilize, leading to the formation of elongated lobes (dotted regions in Fig. 6h). In less than a millisecond, numerous lobes formed across the interphase boundary, elongated and became narrower. Some of these elongated lobes contained small cavitation bubbles that possibly detached from within the droplet and pierced through the interface, becoming arrested (indicated by blue arrows) at $t = 6.375$ ms. At $t = 7$ ms, lobes of different sizes and shapes continued to evolve, with some rupturing from the edges of the horn surface, resulting in the formation of stretched ligament sheets ejecting from the liquid-air interface at velocities in the range of 2 – 12 m/s. Finally, at $t = 9.875$ ms, all the lobes ruptured, forming smaller round droplets (indicated by dotted circles in red) ejected at much lower speeds of 1.25 ± 0.1 m/s compared to stretched ligaments. As the atomization progressed and the remaining liquid film thickness decreased, the droplet size became smaller (until $t = 11.275$ ms). At $t = 12.325$ ms, as the atomization further advanced, the capillary wave patterns can be observed forming on the horn surface. Shortly after at around $t = 12.725$ ms, the capillary waves became distorted and ruptured, generating finer droplets. The atomization process completed when the liquid film dropped below the threshold thickness required for atomization ($t \approx 16.8$ ms). It was not possible to determine the exact threshold thickness in this case. However, the threshold thickness for atomization in case of water at 20 kHz has been found to be almost 50 μm [50]. Thus, for a viscous liquid, this thickness is likely to be higher.

Supplementary material related to this article can be found online at doi:10.1016/j.addma.2024.104033.

The observations of the atomization of a resting drop clearly demonstrated the occurrence of cavitation events within the liquid droplet. The cavitation bubbles grew and collapse, generating high-speed liquid jets and possibly SWs that disrupted the liquid-air interface and caused the droplet to break up into smaller droplets. The size and velocity of the droplets produced was found to depend on the thickness of the droplet. In the case of glycerol, the high viscosity of the liquid prevented the formation of capillary waves. Instead, the increased inertial cavitation activity within the droplet caused the formation of elongated lobes that developed into stretched ligaments and eventually ruptured, producing mist/droplets.

3.1.2. Stabilized liquid film

After studying the atomization dynamics of a single resting drop, we now turn our attention to a stable liquid film (water) on a vibrating plate.

Fig. 7 (and Supplementary Video 3) shows an image sequence of the atomization of a thin liquid film on a vibrating plate at 60% input power. At $t = 0$, the image shows the presence of a stable film of thickness approx. 1 mm. When the ultrasound was turned on, the formation of the first antinode occurred at the far end of the plate, away from the fixed end (encircled in red in Fig. 7b). Subsequently, the development of multiple nodes and antinodes across the length and width of the plate was observed (from $t = 13.4$–35.31 ms). Note that the distance between the two antinodes formed on the plate was roughly similar to the distance observed from amplitude measurements along the length using a vibrometer (see Fig. A1a), any minute variation could be a result of loading the plate with the liquid. Along with the antinodes on the plate (indicated with red arrows in Fig. 7c), the surface capillary waves (or Faraday ripples) [51] also appeared. The formed capillary waves of wavelength ranged from 140 to 400 μm while propagating at speeds of 1.3 ± 0.2 m/s. At $t = 50.85$ ms, the first indication of atomized droplets
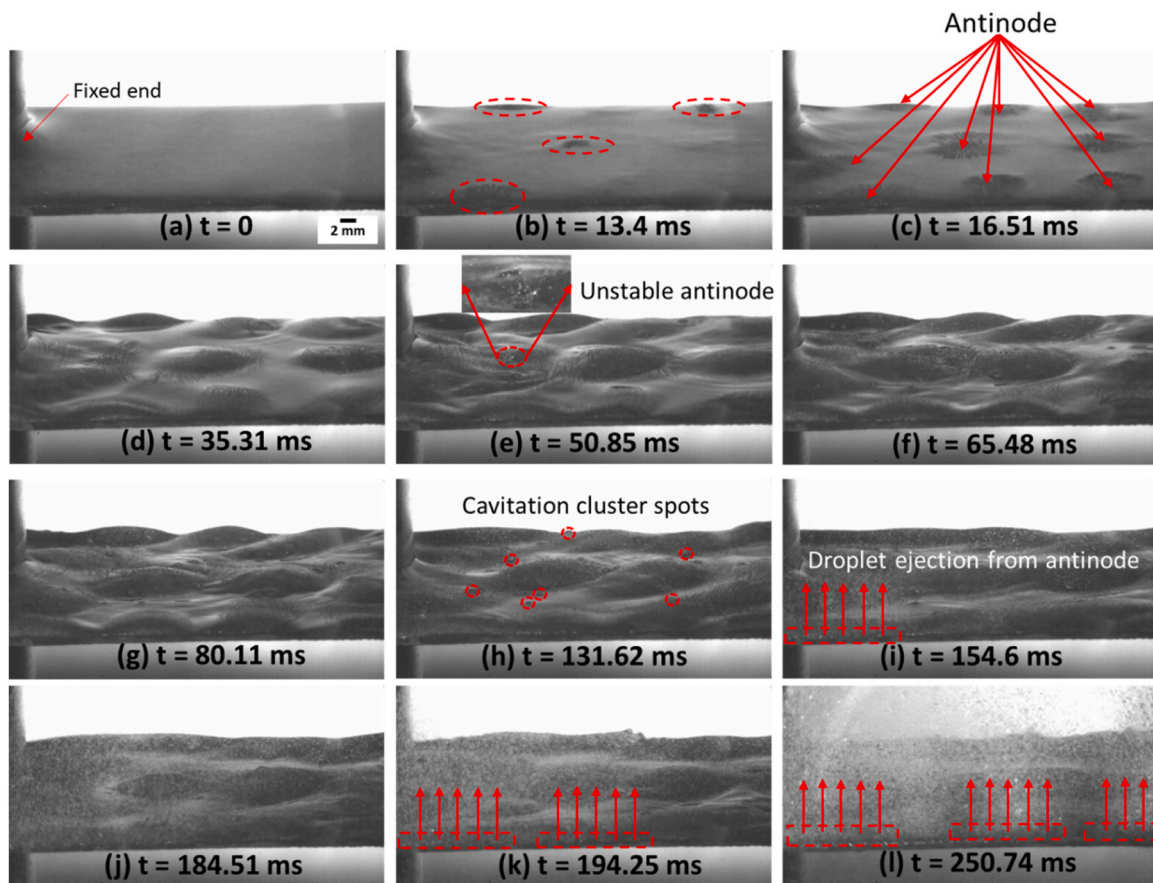

Fig. 7. High-speed images showing initial atomization sequence of a liquid film on a plate captured at an acquisition rate of 35 kHz. See Supplementary Videos 3 and 4.

could be seen as ejections from an unstable antinodal spot with oscillating microbubble clusters (see magnified region on the plate and refer to Supplementary Video 3 for clarity). With the increase in acoustic cycles, several other small spots of cavitation clusters (marked by red circles) also formed across the liquid film (from $t = 50.85–131.62$ ms) and began to eject droplets. It is interesting to note that as soon as the liquid film covered and wetted the side edge near to the fixed end of the plate (see dashed red box), ejection of droplets began (Fig. 7i). Subsequently, the atomization proceeded at each antinodal locations across the plate edge (from fixed end to free end) as shown in Fig. 7(j-l). Supplementary Video 4 shows the initial stages of film atomization captured at acquisition rate of 40 kHz for the 20% input power.

Supplementary material related to this article can be found online at doi:10.1016/j.addma.2024.104033.

In Fig. 7 and Supplementary Videos 3 and 4, the droplet formation mechanism was not as clearly observed as in the case of the single droplet due to insufficient illumination. Thus, the imaging was conducted from a different viewing angle to ascertain the process mechanism (refer to Fig. A2). It was found that the formation and vigorous oscillations of cavities and microscopic air bubbles underneath the liquid layer occur in the center of the antinode of vibration [40], facilitating the formation of capillary waves. The description related to image sequence (Fig. A2) and associated videos can be found in the Appendix.

Supplementary material related to this article can be found online at doi:10.1016/j.addma.2024.104033.

To clarify the role of the cavitation in the generation of nodes/antinodes and capillary waves, another atomization experiment was conducted, using a thicker liquid (water) layer on the plate (refer to Fig. 8(a-f) and Supplementary Video 7). Although this image and video sequence did not show full atomization due to the limited recording duration, Supplementary Video 8 provided a demonstration of the droplet formation. In the first frame ($t = 0$), a stable liquid film with a maximum thickness of 6 mm was observed, containing numerous microscopic air bubbles as shown in Fig. 8a. When the ultrasound was turned on, these cavities started to oscillate and coalesce to form microbubble clusters (see Fig. 8b). With the development of cavitating bubbles, capillary waves also formed close to the bottom edge of the vibrating plate surface (Fig. 8c). Subsequently, the microbubble clusters further grouped together underneath the liquid layer giving rise to the regions characterized by antinodes (Fig. 8(d-f)). It is worth noting that the cavitation activity became more intense over time in the areas of antinode vibration, causing the capillary waves across the liquid surface to become distorted. Droplet ejection subsequently occurred predominantly from the lateral edges of the plate, which also corresponds to the maximum

amplitude as per Fig. A1b. These observations align with earlier investigations [52,53]. It has been previously reported that vibrating a plate immersed in liquid generates capillary waves on the liquid surface, including near the plate edges. The plate vibrations modulate these waves, creating Faraday ripples. The oscillations alter the liquid layer curvature (see Fig. 8(d-f)) and induce surface eddy flows (Fig. A2). The combined effects of inertial cavitation activity within the antinode regions and the capillary forces result in periodic detachment of liquid particles, forming mist/droplets.

Fig. 9 and Supplementary Video 9 demonstrated another interesting evidence that reconfirms the role of cavitation in liquid atomization as was seen in the case of resting drop atomization. Fig. 9a shows the portion of stable liquid (water) film at rest on the plate ($t = 0$). Once the ultrasound was switched on, ripple started to form at $t = 5.7$ ms (marked with dashed blue rectangle). Until $t = 129.7$ ms, the Faraday ripples further expanded across the antinode region (see yellow dashed rectangle). Simultaneously microbubble clouds (seen as small dashed blue circles) with diameter of the order of 300 μm also developed within the water film and moved vigorously across the plate surface due to generated acoustic streaming resembling the characteristics of a swirling bubbly typhoon (refer to Supplementary Video 9). The moment they reached the regions of pressure antinode, they get trapped and start to eject droplets with velocities as high as 2 m/s ($t = 135.8–191.1$ ms). As a result of secondary Bjerknes forces [54–56], defined as the attractive acoustic radiation force between the microbubble clouds, these bubbly typhoons coalesced (Fig. 9j) with each other and propagated predominantly along the lateral edge of the plate and closer to the liquid-air interface. These cavitation (bubbly) swirls could not be observed in case of static drop on horn as well as plate owing to small available surface area for swift movement of microbubble swirls.

Supplementary material related to this article can be found online at doi:10.1016/j.addma.2024.104033.

The observations of a stabilized liquid film demonstrated that atomization process initiates near the lateral edge of the vibrating plate, particularly at the antinode positions. Cavities and air bubbles under the liquid layer was found to oscillate and cluster in antinode locations, facilitating capillary wave formation. These capillary waves are associated with the presence of cavitation swirls within the liquid film. The ejection of droplets occurred as soon as these cavitation swirls streamed towards the antinodal locations.

3.1.3. Single drop impact

Fig. 10 presents a series of images illustrating the atomization process of a single water drop impacting a vibrating plate, captured at an acquisition rate of 50 kHz and 60% input power (see Supplementary
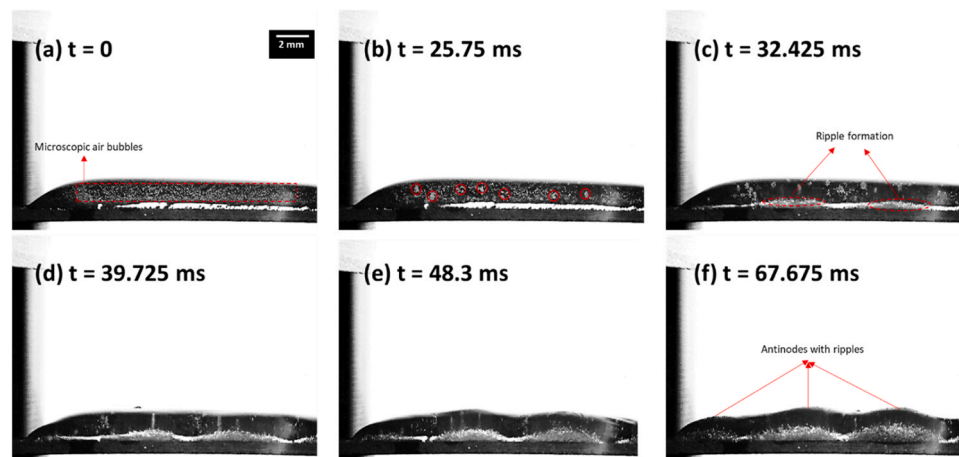

Fig. 8. Sequence of high-speed images showing cavitation activity and induced capillary waves on the antinode regions of a thick film on plate captured at an acquisition rate of 40 kHz. See Supplementary Videos 7 and 8.
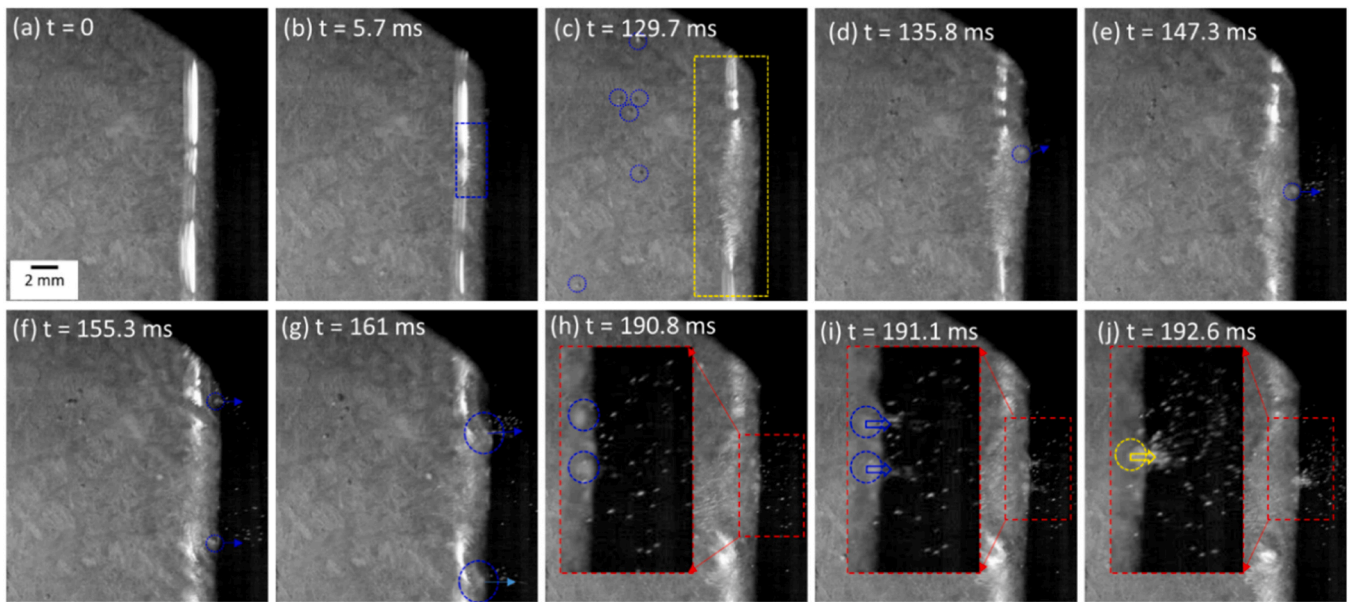
Fig. 9. High-speed image sequence captured at an acquisition rate of 10 kHz showing the effect of swirling bubble typhoons initiating atomization from the lateral edge of the plate. See Supplementary Video 9.
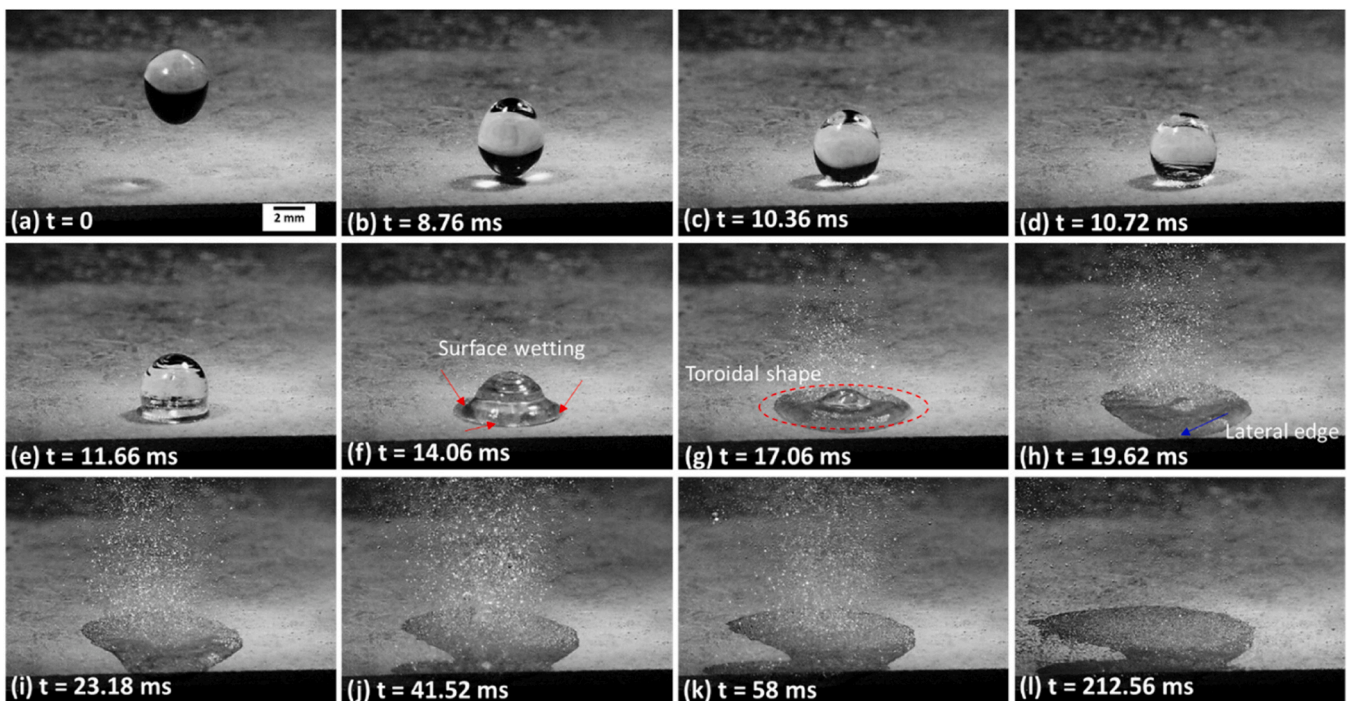

Fig. 10. High-speed image sequence of single water drop impact on vibrating plate captured at an acquisition rate of 50 kHz. See Supplementary Videos 10 and 11.

Video 10). In the first frame ($t = 0$), a spherical drop with a diameter close to 9.5 mm was released from the buret tip positioned about 12 mm away from the vibrating plate. After 8 ms, the drop reached its closest point to the surface (with a velocity of around 0.8 m/s). At $t = 10.72$ ms, the first moment of collision was captured as the drop touched the plate surface. At impact, a capillary wave with a wavelength almost reaching 280 μm, emerged from the bottom and propagated along the droplet surface at speed of ca. 2 m/s. This corresponds to 9 kHz, which was nearly half the driving frequency of the vibrating plate. The impact also deformed the drop into a pyramidal shape. As soon as the deformed drop wet the surface, the thinnest liquid layer in contact (indicated with red

arrows) initiated the droplet atomization (Fig. 10f). This is followed by lateral spreading of the deformed drop, forming a toroidal structure with the central portion of the drop higher than its sides as shown in Fig. 10g. As the thickness decreased of the spread layer and surface wettability increased, atomization intensified and continued until the drop expanded and stretched to its minimum thickness, ceasing atomization.

Supplementary material related to this article can be found online at doi:10.1016/j.addma.2024.104033.

The atomization occurred initially only on one side of the drop. When the other side of the spreading layer reached the lateral edge of the plate at $t = 19.62$ ms (blue arrow), atomization immediately began,

similar to what was observed during film atomization on the plate. At a higher input power, such as 100% (see Supplementary Video 11), atomization started quicker upon drop impact, most likely due to a larger momentum transfer from the plate to the drop surface. Under the higher plate amplitude, unlike at the lower amplitude, no drop deformation (shape changes) and development of capillary waves was observed upon the drop impact possibly due to almost instant atomization. In both cases, the atomization proceeded from the spread layer that wetted the plate. However, at the higher amplitude, the wet surface zones were more confined to smaller areas around the drop. Finally, the central portion of the mother (primary) drop was the last portion to atomize.

Supplementary material related to this article can be found online at doi:10.1016/j.addma.2024.104033.

Although the macro-scale atomization process can be partially understood through the generation of capillary waves, it is challenging to establish or confirm, based on the provided image sequences, whether cavitation still dictates the breakup mechanism of primary drops during impact. Therefore, to investigate this further, a glycerol drop was used as a medium for studying the drop impact mechanism on a horn (due to larger vibration amplitude) instead of a plate.

Fig. 11 illustrates a series of images showing the impact of a single glycerol drop on the tip of an ultrasonic horn vibrating at 100% input power. The complete atomization sequence can be observed in Supplementary Video 12. Fig. 11a shows a glycerol drop with a diameter of ca. 4 mm under a free fall with a velocity of 1.5 m/s. At $t = 2.77$ ms, the drop impacted the horn surface. Upon impact, a cylindrical column with a mushroom-like shape developed due to the suction effect from the vibrating horn (Fig. 11b, enclosed region in red). Immediately after, the first ejection of atomized mist from the primary drop could be observed (enclosed regions in red in Fig. 11c) also termed as "edge splash" elsewhere [10]. After 1 ms, cavities formed on the bottom surface close to the horn. From $t = 3.02$–3.08 ms (refer to Supplementary Video 12), the cavitation bubble grew and underwent implosion upon 1–2 acoustic cycles. The bubble oscillating period prior to collapse was found to be from $t = 3.17$–3.31 ms and $t = 3.31$–3.45 ms. The bubble then attained its maximum size at $t = 3.37$ ms before collapsing at 3.45 ms. This corresponded to periodic implosions occurring every $1/3^{rd}$ of the driving

frequency as a result of non-collapsing deflations [57], thus confirming the role of inertial cavitation in the atomization process. The collapse of the cavity was followed simultaneously by the release of numerous secondary droplets also termed as "surface splash". As the same time, the cavitating bubble also underwent splitting, forming cavitation bubble clusters with a diameter of roughly 1.5 mm at $t = 3.54$ ms. With the increased aggressiveness of cavitation activity, the primary drop started to deform/compress, leading to surface distortions and spreading the interphase boundary region ($t = 5$ ms). This was then followed by the expansion of the drop over the horn tip with atomization subsequently progressing in a similar fashion as observed earlier in Fig. 6(g-o). Droplet formation subsequently occurred from the pinching-off of the stretched ligament sheets ejecting at velocities up to 12 m/s (refer to Supplementary Video 12) implying the effect of high-speed liquid jets from energetic subharmonic cavitation collapses as also shown in Fig. 6.

Supplementary material related to this article can be found online at doi:10.1016/j.addma.2024.104033.

Thus, the observations of a single drop impact clearly demonstrated the role of capillary waves and wet surface conditions in initiating and intensifying atomization. This mechanism was observed along the periphery of the drop, leading to efficient atomization. Higher input power accelerated atomization upon impact. The experiment using glycerol on a vibrating horn reaffirmed the presence of inertial cavitation in generating secondary droplets through energetic collapses.

While high-speed optical imaging revealed the process mechanism for each given case of liquid atomization, providing clear evidence of cavitation and the generation and breakup of capillary waves at a meso scale, the dynamics of cavitation activity and its effect on the generation of capillary waves, their wavelength and droplet size remain unclear. In the following section, we present and discuss the results obtained from ultrafast synchrotron X-ray imaging of single droplet impact atomization experiments performed at the Advanced Photon Source in Chicago, USA. These experiments allowed us to shed light on the atomization process on a micro scale, further strengthening the aforementioned results and discussion.
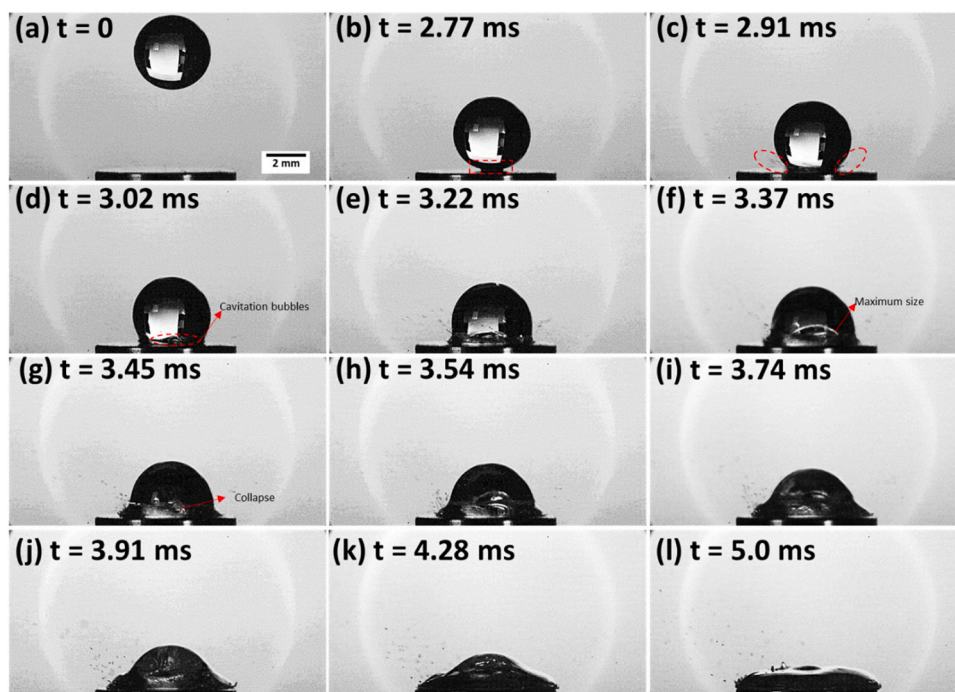

Fig. 11. High-speed images showing the atomization sequence of a glycerol drop impact on a horn captured at an acquisition rate of 35 kHz. See Supplementary Video 12.

3.2. Ultrafast synchrotron X-ray imaging results

Fig. 12a, together with the Supplementary Video 13, provides a detailed temporal image sequence, unveiling the onset of the atomization process. At an operating condition of 20% input power and a peak-peak amplitude of 16 μm, the idle state of the sonotrode tip with a statically resting drop is shown by the frame (a1) at $t = 0$ ms. Subsequently, upon ultrasound triggering, heterogeneous nucleation of microscopic bubbles occurred on the surface, ranging in size from 45 μm to 70 μm. These bubbles underwent pulsation, characterized by repetitive growth and collapse. As the process advanced, coalescence of the bubbles took place, forming clusters of microbubbles with size approaching 200 μm, which populated along the horn surface similar to the phenomena seen in Fig. 6 (and Supplementary Video 2).

Supplementary material related to this article can be found online at doi:10.1016/j.addma.2024.104033.

At $t = 1.46$ ms, capillary waves began to form and propagate across the liquid-air interface at velocities in the range of 1.2 – 1.8 m/s, as shown in Fig. 12(a5). With further bubble growth, oscillations, and implosions, the capillary waves became more pronounced throughout the field of view, as depicted in Fig. 12(a6). However, as the capillary waves interacted with regions near bubble implosions, distortion became evident, as seen in Fig. 12(a5-a8). Consequently, capillary wave instability manifested through the distortion of the interphase boundary, observed in Fig. 12(a8) as droplets (ca. 42 ± 10 μm in size) started to pinch-off from the crests formed on the capillary waves along the interphase boundary region at $t = 2.08$ ms (Fig. 12(a10)). The observed crest distortions can be correlated with the stretching of the ligament (liquid) sheets (refer to Figs. 6 and 11 and associated Supplementary Videos 2 and 12, respectively) with velocities of 12 ± 4 m/s. The droplet pinch-off in water occurred much faster than in glycerol. Notably, not every crest region of the unstable capillary waves pinched off to form a droplet simultaneously, indicating the complexity and stochastic nature of the process, depending mainly upon the intensity of the cavitation
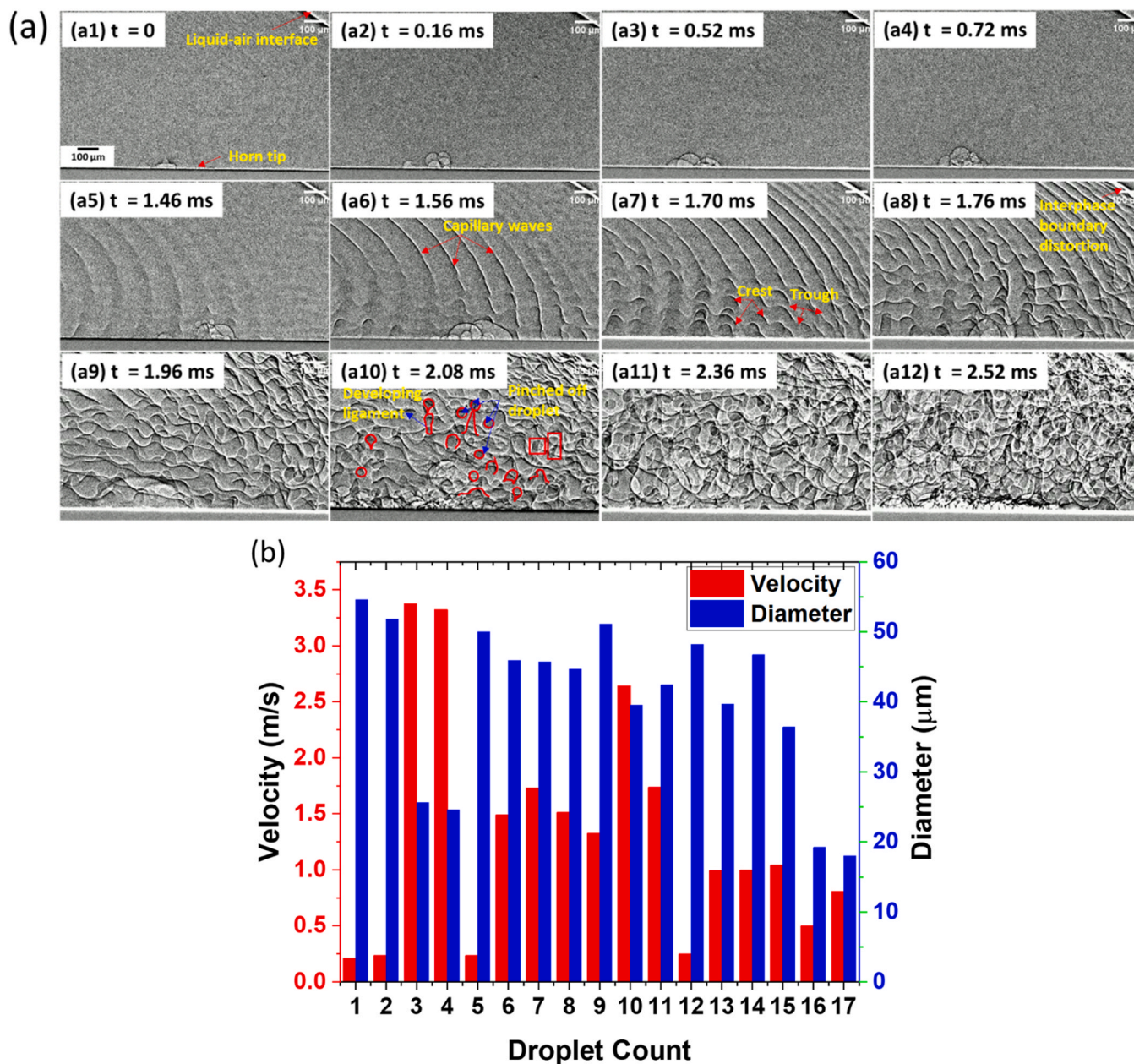

Fig. 12. (a) Ultrafast synchrotron X-ray images, showing the atomization sequence of a water droplet impacting the horn captured at an image acquisition speed of 50 kHz. See Supplementary Videos 13 and 14. (b) Estimated diameter and velocity of atomized droplets obtained from Supplementary Video 15.

activity.

Continuing the observation from t = 2.08–2.48 ms, the liquid-air interface across the entire droplet surface became highly unstable, leading to the formation of multiple droplets, accompanied by ongoing cavitation events. Within this sequence, fully formed capillary waves were observed before the formation of secondary droplets (from t = 1.46–2.08 ms). The excitation frequency gave rise to surface waves with a capillary wavelength (λ) of 100 ± 10 μm, reasonably close to the theoretical wavelength of ~80 μm calculated using Kelvin's equation:λ $= \left(2\pi\sigma/\rho f^2\right)^{1/3}$ [58,59], where σ represents the liquid's surface tension, ρ is the density, and f is the driving frequency of the ultrasound. Moreover, the size of the initially ejected droplets was found to be nearly half the wavelength of the propagating capillary waves with secondary droplets primarily originating from crest regions across the unstable waves [60]. It was challenging to derive the atomized droplet size and velocity through image processing due to the complex interaction between cavitation bubble, pinch-off droplets and capillary waves as seen in Supplementary Videos 13 and 14. Therefore we used Supplementary Video 15 to estimate the velocity and diameter of some of the atomized droplets as shown in Fig. 12b. It can be seen that the droplet size varied in the range of 40 and 50 μm, while velocity was found to be varying from as low as 0.2–3 m/s. Interestingly, the stretched ligaments traveled at velocities as high as 10 m/s (refer to Supplementary Videos 14 and 15) similar to observations made in case of glycerol, thus reinforcing the role of liquid jets and SWs generated from transient bubble collapses, thus triggering the atomization process. These velocities were also closer to the range observed in case of resting drop atomization (Fig. 5).

From the measured propagation speed and wavelength of capillary waves formed across the liquid-air interface, it can be confirmed that the corresponding frequency is almost half of the driving frequency. Refer to Table A2 in Appendix, which shows the frequencies of the unstable surface waves measured both experimentally and theoretically using Kelvin's equation for all the atomization scenarios. It can be seen that the measured frequencies are in close agreement with the theoretically predicted frequency values. Although, the frequency of waves during the stable phase of the capillary motion is same as the excitation frequency, which also exist for very small vibration amplitudes. However, as the waves become unstable, the frequency of motion becomes subharmonic in nature based on the Faraday instability criterion [22,61–63]. It can be seen from the table that the frequencies of these waves exhibit several subharmonic modes, i.e. $f/2$, $f/3$, $f/4$, $f/5$ and $f/7$, where f is the driving frequency of the transducer. The appearance of these subharmonics as a result of non-collapsing deflations of bubble cloud could be an indication of SWs interaction with the liquid-air interface [48]. Simultaneously, the oscillation/collapse rate of microbubble clusters also shifted from close to fundamental to subharmonic frequencies (almost 1/3 of the driving frequency) prior to the formation of secondary droplets. For example, the cavitation activity occurring between t = 1.14–1.24 ms, which corresponds to implosions occurring every 3 acoustic cycles (refer to Supplementary Video 13). The shift in bubble growth/collapse frequency can also be visualized in Supplementary Video 14. Previous studies have shown that subharmonic collapses are powerful in nature and can generate high-intensity liquid jets and SWs [48,57,64,65]. Presumably, these jets and the impending SWs upon interacting with the stable wave-dominated interphase boundary, result in capillary distortion, subsequently leading to the formation of crest and trough regions that rupture, ultimately giving rise to atomized droplets. However, further investigation is needed to confirm this premise and will be the focus of our future work.

Supplementary material related to this article can be found online at doi:10.1016/j.addma.2024.104033.

The X-ray images/videos unequivocally demonstrated that ultrasonic atomization involves a series of dynamic phenomena, including (sequentially) cavitation nucleation, bubble pulsation, coalescence, splitting, and the formation of capillary waves. The initial regime entailed the nucleation of multiple bubbles within the primary droplet, facilitated by the growth and collapse cycle of the bubbles. This was followed by their merging to form large microbubble clusters. Subsequently, capillary waves developed on the liquid-air interface. Upon the collapse of cavitation bubbles, formation of stretched ligaments occurred, which underwent pinch-off, resulting in the generation of one or more secondary droplets.

3.3. Stages of atomization evolution

Utilizing a combination of advanced high-speed optical and ultrafast X-ray imaging techniques, we have obtained unique insights into the intricacies and dynamics of ultrasonic atomization. These imaging observations allowed us to reveal the internal structure and phenomena associated with droplet formation, effectively resolving any ambiguities present in the existing literature. As depicted in Figs. 4–12 along with Fig. A2 in Appendix, our observations conclusively demonstrated that ultrasonic atomization is governed by the interplay of the capillary and cavitation wave theory, with dynamic cavitation events driving the overall process.

To elucidate the sequential stages of atomization for resting drops or films, we present a schematic in Fig. 13. Initially (Stage 1), the liquid surface remains undisturbed, hosting pre-existing cavities within the drop or film. With the introduction of ultrasonic waves (Stage 2), localized regions of low pressure emerge, prompting the growth and pulsation of small pre-existing gas/air bubbles. At this point, the liquid surface maintains its smoothness, with only a smaller population of bubbles. As cavitation activity intensifies (Stage 3), the number and size of bubbles increase, resulting in the formation of clustered bubble clouds. In Stage 4, these microbubble clusters undergo implosions, continuously splitting and oscillating in shape, generating SWs and liquid jets. The bubble clouds expand, occupying a significant portion of the liquid volume. In Stage 5, capillary waves emerge on the liquid surface, indicating the interaction between cavitating bubbles with the liquid/air interphase boundary. As mentioned earlier, direct observation of SWs and high-speed liquid jets interaction was not feasible in our experiments, yet using the same experimental setup under similar conditions, we have previously monitored the propagation of SWs after every implosion of the bubble cloud in [66]. Thus, it is reasonable to infer that high velocities of 10 – 12 m/s in highly viscous liquids such as glycerol (refer to Fig. 11 and Supplementary Video 12) are a direct consequence of the rapid movement of liquid jets emitted from clusters of highly energetic inertial cavitation microbubbles. These liquid jets are believed to be followed by the propagation of SWs [44]. Interestingly, in the case of the plate setup, the formation of swirling cavitating bubbly typhoons migrate with acoustic streaming was noticed ejecting tiny droplets close to the edge of the plate further promoting atomization. As the interaction intensifies, the capillary waves distort, giving rise to crest and trough regions along the liquid-air interface (Stage 6). This distortion initiates near the solid-liquid interface in the antinodal regions, where cavitation events exhibit more aggressive behavior. Eventually, the rupturing and pinching-off of crest regions occur, leading to the formation of larger atomized droplets (Stage 7) followed by the formation of a cloud-like mist that disperses and spreads. Simultaneously, the liquid volume expands along the surface (lateral spreading), wetting a larger area. The atomization process persists until the liquid film thickness falls below a critical threshold (Stage 8).

Droplet impact on a vibrating surface introduces complexity, leading to phenomena involving capillary waves, surface splash, edge splash, and sub-droplet rebound. While some aspects from non-vibrating surfaces apply, such as Weber number (We) influence, vibrating surfaces add unique features, affecting liquid film spreading, capillary waves, and droplet ejection. Renardy et al. [67] found that We < 1 results in minimal deformation, while We > 1 causes spreading and potential splashing. For We exceeding approximately 4, capillary waves form a pyramid structure; drops with We > 1 exhibit pyramidal shapes,
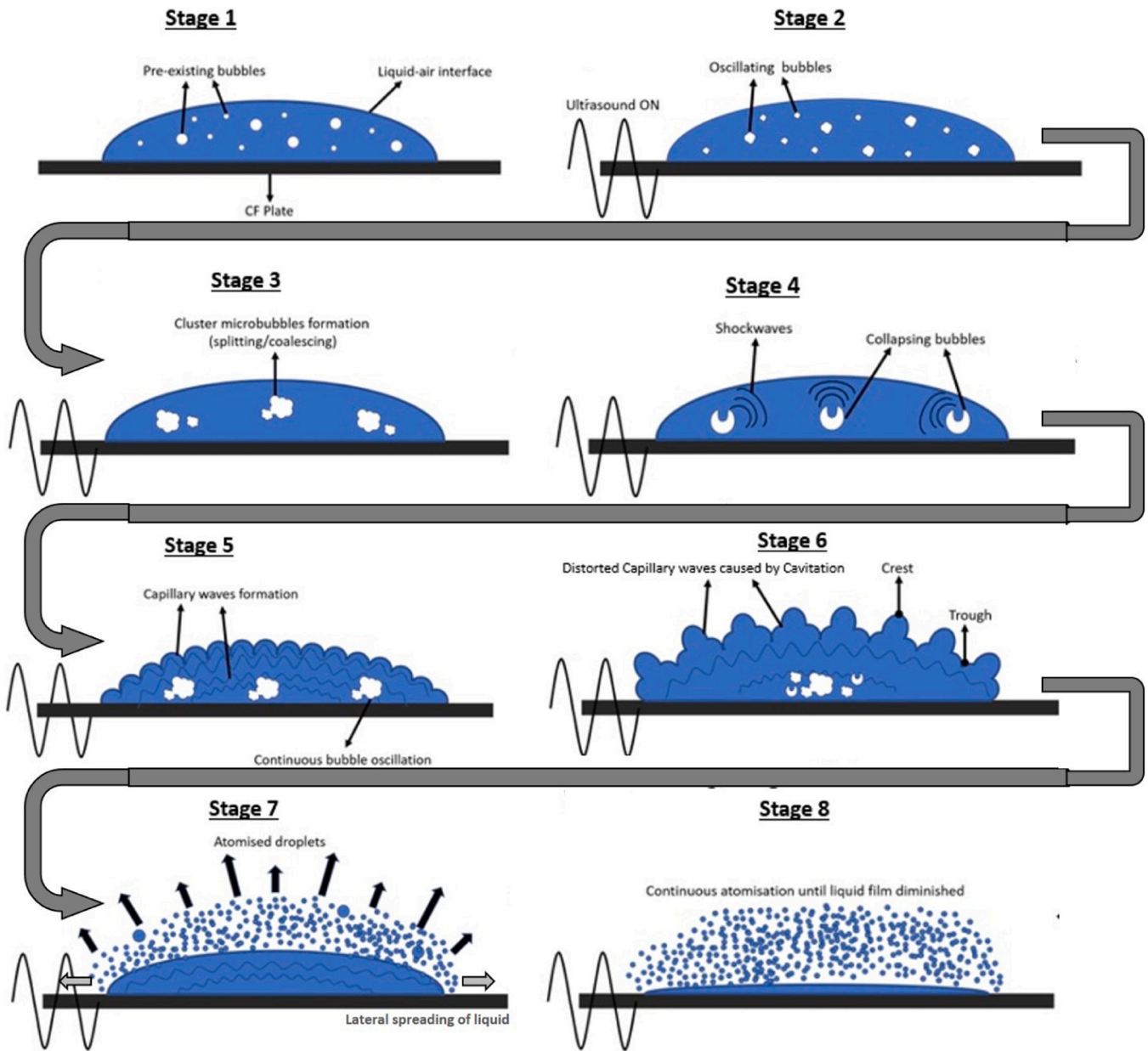
Fig. 13. Schematic representation showing the stages (left to right) of ultrasonic atomization of a liquid drop/film resting on vibrating plate.

followed by toroidal formation and lift-off from the substrate. The interplay of mechanical vibrations, surface tension, and fluid properties further influences droplet impact dynamics on a vibrating surface. Fig. 14 provides a schematic representation of the sequential steps governing droplet impact atomization. The principal dynamics of this process remains governed by the cavitation-wave theory, as evident from Figs. 10–12 and the accompanying Supplementary Videos. Upon collision with the vibrating horn/plate, the droplet forms a contact layer, followed by the ejection of liquid jets "edge splash" from this layer. Pre-existing air or vapor cavities develop within the primary droplet, oscillating, merging and splitting before collapsing violently. Concurrently, capillary waves arise at the edge of the liquid film/drop, propagated towards the center. Throughout this process, cavitation events intensify with vigorous collapses, leading to the formation of crest-and-trough regions along the liquid-air interphase boundary, as shown in Fig. 12(a7) and schematically depicted in Fig. 13. These cavitation-induced distortions ultimately result in the rupture and pinching-off of crest (ligament) regions, generating fine droplets (Fig. 12

(a12)). The liquid droplet spreads across the vibrating horn/ plate, wetting the surface and causing surface splashing. The final step involves the splashing of the wetted layer across the vibrating plate, followed by sub-droplet rebound [10], where capillary waves congregate at the central portion of the droplet. This represents the last stage of droplet atomization, as illustrated in the Supplementary Video 10. The degree of splashing varies depending on the excitation amplitude, ranging from pronounced to minimal. In certain cases, the entire droplet volume can be ejected [11]. The transition from stable capillary waves to distorted (unstable) waves, resulting in droplet atomization, is solely dependent on the vibration amplitude rather than the droplet's impact velocity. However, both amplitude and impact velocity can influence the intensity of the splash. Supplementary Videos 10 and 11 provide visual demonstrations of the contrasting splashing behavior resulting from changes in amplitude. It is important to note here that capillary waves form at the liquid surface only after the cavitation activity has been initiated as observed from synchrotron studies. As the cavitation activity becomes aggressive, these waves develop crests and troughs
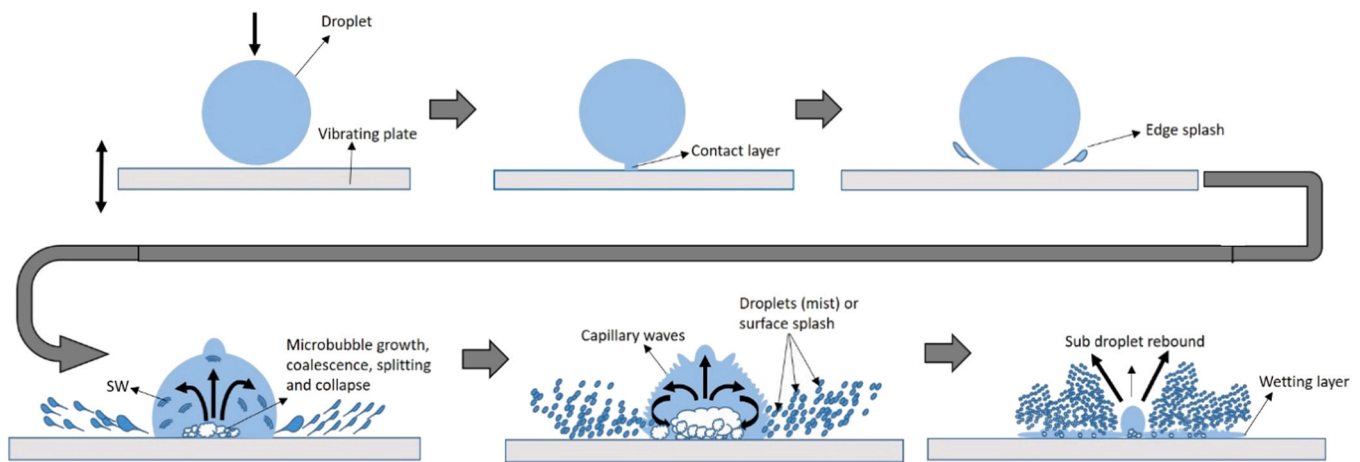
Fig. 14. Schematic representation showing the evolution sequence of ultrasonic atomization of a liquid drop impact on vibrating horn/plate.

following the pinching-off of droplets from the stretched ligaments sheets.

3.4. Ultrasonic atomization of pure aluminum

Following the fundamental studies of atomization in transparent liquids at room temperature, next step is to apply similar technique to understand the atomization in liquid aluminum [38]. This is of great technological importance due to direct application in generating feedstock for additive manufacturing processes. As previously mentioned, the choice of water in this study was dictated by its similar properties to those of liquid aluminum. Manufacturing aluminum powders is a challenge that can be addressed by ultrasonic atomization as demonstrated here. Fig. 15 shows the measured volumetric particle size distribution (PSD) of produced aluminum powders at constant frequency of 60 kHz and various input powers (amplitudes) of 60, 75 and 100%. Note, the frequency used for these experiments were higher than the frequencies used during transparent liquids atomization (20 – 30 kHz). In contrast to the conventional Gaussian PSD observed in commercial feedstocks for additive manufacturing [68], our study reveals a positively skewed distribution. This departure from the traditional distribution may be attributed to a higher concentration of finer particles, which has been reported to enhance the powder packing density [69]. This modified distribution could most likely be the result of slow pouring of the Al melt ($\sim$50 cm^3/min), which effectively maximizes the quantity of finer particles as larger stream of molten metal results in coarser particles. It is also important to note here that the process itself does not produce
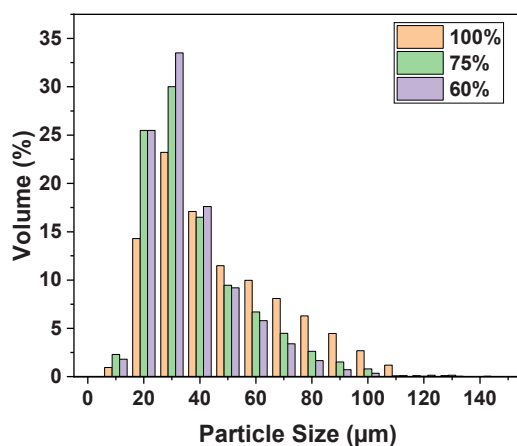

Fig. 15. Particle size distribution of ultrasonically atomized Aluminum (99.9%) with various amplitudes 100, 75 and 60%.

powders below 10 μm, minimizing the deviations observed in finer particles. Based on the experimental and numerical simulations, it has been found that the atomized droplet size varies in range of 20 – 30 μm when driving frequency increased from 20 to 60 kHz [50,70,71]. The results of particle size analysis using laser diffraction are shown in Table A3. The table clearly demonstrates that increasing the input power (amplitude) significantly influences the PSD, as previously observed in Fig. 5, where varying the thickness of the liquid dome resulted in different droplet sizes. A lower input power led to more efficient atomization, breaking the liquid aluminum into smaller droplets that solidify into finer particles. This observation aligns with the findings for thinner film thickness, where Fig. 5 illustrated the production of a finer population of droplets. Moreover, increased power can also lead to a more aggressive cavitation activity within the liquid film, forming larger bubbles and subsequently larger droplets.

Another aspect to consider is the uniformity of the PSD. At 100% input power, the span between D_{10} and D_{90} is 67.6 μm, while at 60% input power, it reduces to 21.8 μm. This indicates that lower input power results in a narrower PSD, with less variation between the smallest and largest particles. The difference in particle size for 75% and 100% amplitude is significant, while between 60% and 75%, it is minimal or within the limit of measurement error, which may indicate that a certain threshold level has been reached for a selected group of particles below which any further reduction of amplitude has no effect on the quality and size of the powder produced. The data in the Table A3 can be valuable for process optimization. Depending on the application requirements, the input power level can be adjusted to control the particle size and distribution. It also highlights the trade-off between particle size and its uniformity, allowing for better process control and optimization based on the specific needs of different applications. For example, in applications where a narrow particle size distribution is crucial, a lower input power and lower liquid film thickness might be preferred to achieve a more uniform product. Conversely, if a higher count of smaller particles is desired, a higher input power level would be more appropriate. However, this may require an additional step of sieving to retrieve only the smaller particles.

Fig. 16(a-c) displays scanning electron microscope (SEM) images of powders generated at various amplitudes. While there are notable differences in particle size across the images, the powders exhibit strikingly similar characteristics. Specifically, they demonstrated exceptional sphericity and an absence of elongated or clustered particles. It is important to note here the atomized powder did not contain any trapped gas pores as shown in Fig. 16d. This attribute is particularly beneficial for AM process, where smooth and consistent material flow is crucial for producing 3D printed components with high bulk density. Additionally, the absence of satellites in the produced powders ensures a more
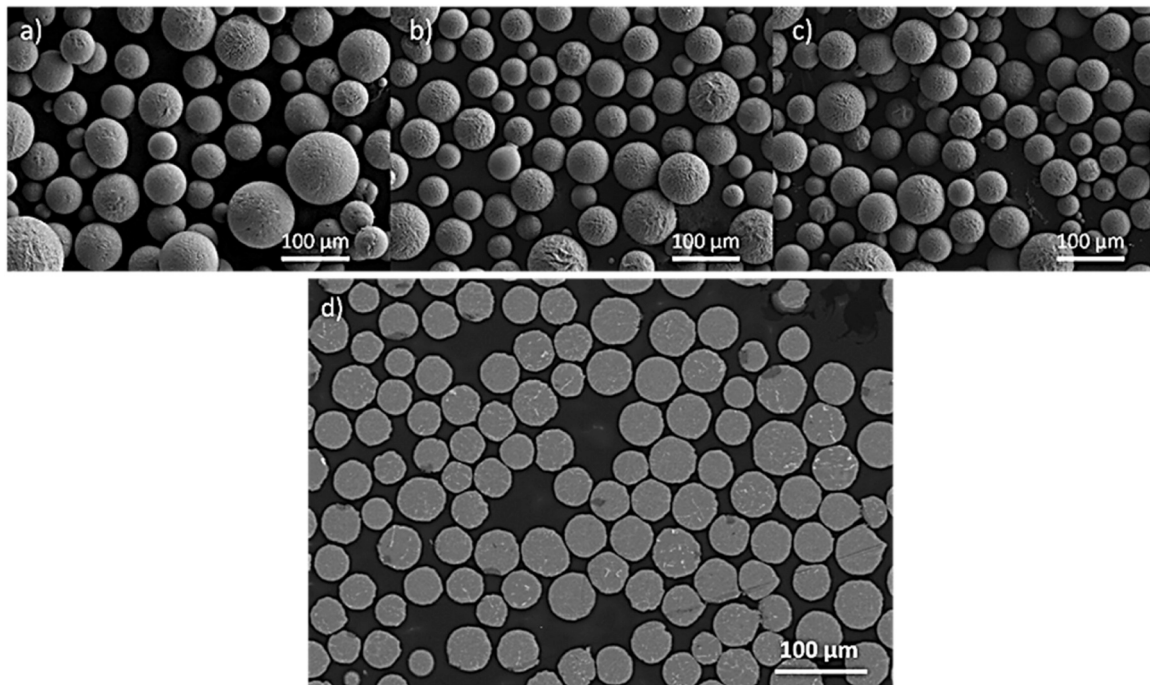
Fig. 16. SEM images of ultrasonically atomized Aluminum (99.9%) with various amplitudes (a) 100%, (b) 75%, (c) 60% and (d) showing typical cross-section of the produced particles free of trapped pores.

homogeneous feedstock, contributing to the reliability and repeatability of the 3D printing process. Furthermore, the narrow PSD is particularly advantageous for certain AM techniques, such as laser powder bed fusion (LPBF) technology [72,73]. In LPBF, a tight control over particle size distribution is crucial for achieving high-resolution prints with excellent mechanical properties. Thus, apart from frequency [9,74] the vibrating amplitude as well as the film thickness and wetting has been identified as another crucial parameter that influences the PSD of the produced droplets/powders during ultrasonic atomization.

4. Conclusions

In situ studies of ultrasonic atomization of water droplets on a vibrating plate and a horn surface have been conducted using high-speed optical and ultrafast synchrotron X-ray imaging. Additional experiments with glycerol were also performed to study more specific aspects of the process. The feasibility of ultrasonic atomization of liquid aluminum using this technology was also demonstrated in addition to the fundamental studies. The *in situ* observation revealed the critical role of cavitation in contributing to the atomization process in different scenarios:

1. Capillary waves were formed as a direct result of cavitation and cavitation played a disruptive role in the fragmentation of Faraday ripples and facilitated droplet formation through the pinching-off of ligament edges.
2. Cavitation also produces bubbly typhoon swirl streaming flow, which is the crucial intermediate step in the overall atomization process.
3. Cavitation-induced shock waves are the driving force for capillary formation and the propagation of SWs triggered the disruptions of the liquid dome. The periodicity of shock waves (indicated by the subharmonics) were found to align with the wavelengths of the distorted capillary waves.
4. Processing relationships between the liquid film thickness, wetting and vibration amplitude and the resulting liquid droplets (particles)

size, morphology and distribution of the ultrasonically atomized molten aluminum were also further elucidated in this study.

Overall, this study has provided a holistic understanding of ultrasonic atomization, revealing the multifaceted role of cavitation in the intricate processes that govern the formation of atomized droplets and particles.

CRediT authorship contribution statement

Tzanakis Iakovos: Writing – review & editing, Supervision, Funding acquisition. **Fezzaa Kamel:** Data curation, Methodology, Resources. **Lee Peter D.:** Writing – review & editing, Funding acquisition, Supervision. **Eskin Dmitry:** Writing – review & editing, Supervision, Funding acquisition. **Leung Chu Lun Alex:** Writing – review & editing, Funding acquisition, Supervision. **Mi Jiawei:** Writing – review & editing, Supervision, Resources, Methodology, Investigation, Funding acquisition, Data curation, Conceptualization. **Zrodowski Lukasz:** Writing – review & editing, Validation, Resources. **Clark Samuel J.:** Data curation, Methodology, Resources. **Qin Ling:** Visualization, Methodology, Data curation, Investigation. **Shahrani Shazamin Bin:** Visualization, Methodology, Investigation, Data curation. **Choma Tomasz:** Writing – review & editing, Validation, Resources, Methodology, Investigation, Formal analysis. **Priyadarshi Abhinav:** Writing – review & editing, Writing – original draft, Visualization, Validation, Software, Methodology, Investigation, Formal analysis, Data curation, Conceptualization.

Declaration of Competing Interest

The authors declare that they have no known competing financial interests or personal relationships that could have appeared to influence the work reported in this paper.

Data availability

Data will be made available on request.
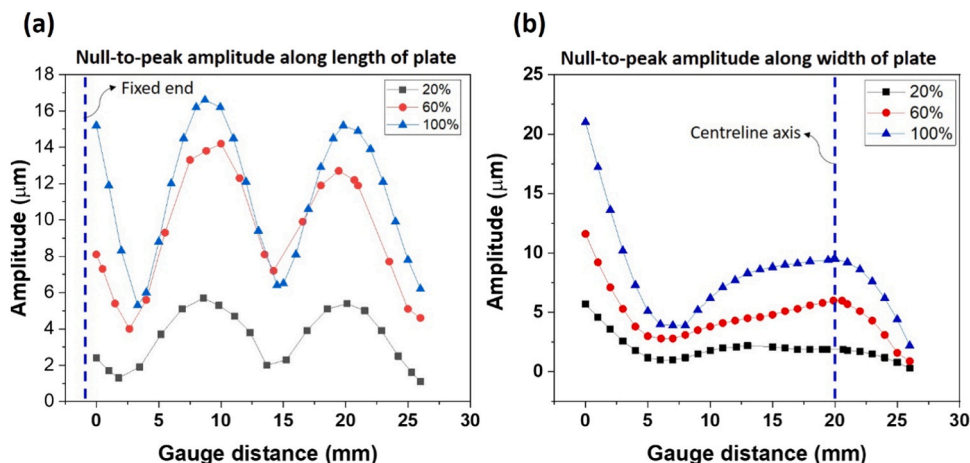
Acknowledgments

Appendix

Fig. A1. Null-to-peak amplitude of the vibrating plate measured along the (a) length and (b) width, using the vibrometer.

.

Fig A2(a-f) and Supplementary Video 5 present the atomization sequence from the top view of the liquid film on the plate captured at acquisition rate of 10 kHz. After turning on the ultrasound, the Faraday ripples started to appear and cover the right edge of the plate. The capillary waves spread further across the plate, with ripples becoming dominant at antinodes (encircled regions in red in Fig. A2c). At $t = 88.9$ ms, the first instance of droplet ejection from the edge of the plate could be observed (indicated by red circles). Atomization primarily occurred from the antinodes formed near the fixed end of the plate until $t = 225.6$ ms. Supplementary Video 6 shows a similar atomization sequence performed at 100% input power, where droplet ejection can be more clearly observed from the disruption of capillary waves formed on the antinodes. It can be deduced from Fig. 7 and A2 that the atomization process initiated over the wetted layer in the vibrating regions closer to the point of plate fixation to the sonotrode, predominantly at the lateral edges of the plate in the presence of antinodes.
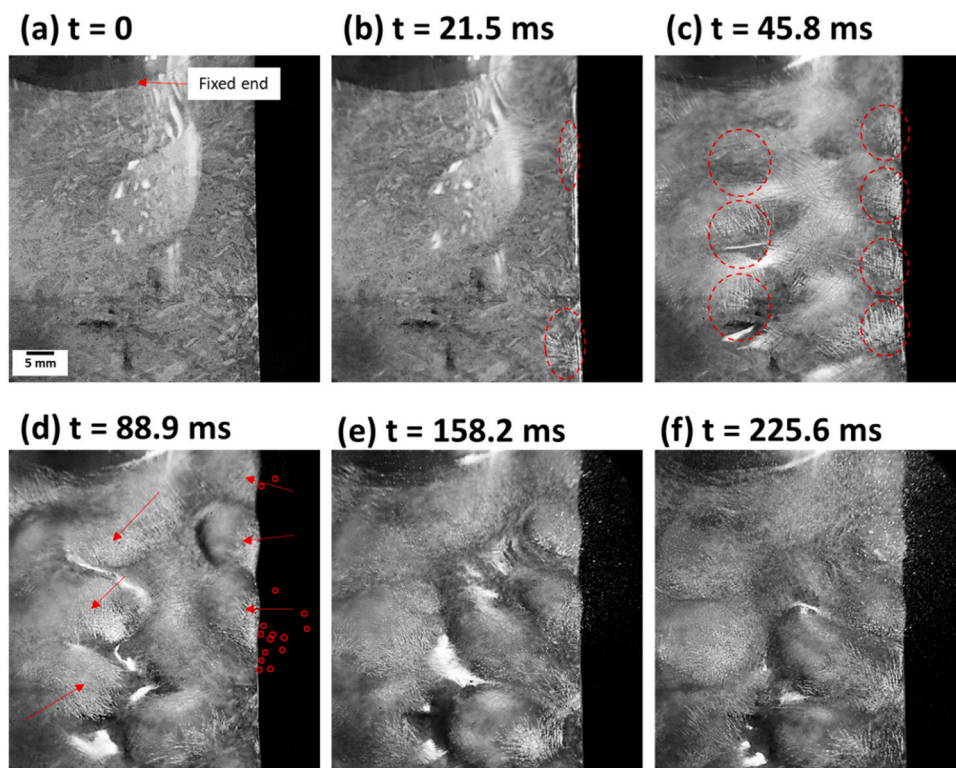
Fig. A2. High-speed images showing atomization sequence from the top view of the film on plate captured at an acquisition rate of 10 kHz. Red dotted circles in (b) and (c) shows the evolution of Faraday ripples starting from the lateral edge of the CF plate. Arrows and small red circles in (d) shows the fully developed antinodes on the plate and first indications of droplet ejections, respectively. See Supplementary Videos 5 and 6.

Table A1

Vibration amplitude of the transducers for different input powers of ultrasound used for liquid atomization.

Input Power Transducer	20%	60%	100%
	Ultrasonic amplitude (μm) peak-to-peak		
UIP500hdT	11.4	34.2	57
UP200S	35	105	175
UP100H	16	48	80

Table A2

Frequency of distorted capillary waves in water estimated experimentally and theoretically for different atomization scenarios.

Atomization type (driving frequency)	Wavelength of distorted wave (μm)	Propagation velocity (m/s)	Measured frequency (kHz)	Theoretical frequency using Kelvin's Eq. (kHz)
Static drop on plate (20 ± 1 kHz)	333 ± 5	1.5 ± 0.3	4.5 ± 0.9	3.6 ± 0.1
Stable film on plate (20 ± 1 kHz)	400 ± 10	1.3 ± 0.3	3.3 ± 0.7	2.8 ± 0.1
Impact drop on plate (20 ± 1 kHz)	280 ± 9	2.0 ± 0.2	7.1 ± 0.8	4.7 ± 0.2
Impact drop on horn (30 ± 1 kHz)	100 ± 10	1.5 ± 0.3	15 ± 3.0	22 ± 0.3

Table A3

Particle size distribution of produced aluminum powders using ultrasonic atomization.

Input power /Amplitude	Volumetric [μm]			Count [μm]		
	Dv_{10}	Dv_{50}	Dv_{90}	D_{10}	D_{50}	D_{90}
100% / 9.9 μm	21.3	41.7	82.8	15.2	24.5	42.7
75% / 9 μm	18.0	32.4	64.4	12,4	22.1	34.9
60% / 8.55 μm	18.2	31.8	59.1	12.8	22.4	34.6

References

[1] W.E. Frazier, Metal additive manufacturing: a review, J. Mater. Eng. Perform. 236 23 (2014) 1917–1928, https://doi.org/10.1007/s11665-014-0958-z.

[2] J. Zhang, B. Song, Q. Wei, D. Bourell, Y. Shi, A review of selective laser melting of aluminum alloys: processing, microstructure, property and developing trends, J. Mater. Sci. Technol. 35 (2019) 270–284, https://doi.org/10.1016/j.jmst.2018.09.004.

[3] W. Nan, M. Pasha, T. Bonakdar, A. Lopez, U. Zafar, S. Nadimi, M. Ghadiri, Jamming during particle spreading in additive manufacturing, Powder Technol. 338 (2018) 253–262, https://doi.org/10.1016/j.powtec.2018.07.030.

[4] M. Ahmed, M. Pasha, W. Nan, M. Ghadiri, A simple method for assessing powder spreadability for additive manufacturing, Powder Technol. 367 (2020) 671–679, https://doi.org/10.1016/j.powtec.2020.04.033.

[5] S.H. Saheb, V.K. Durgam, A. Chandrashekhar, A review on metal powders in additive manufacturing, AIP Conf. Proc. 2281 (2020) 020018, https://doi.org/10.1063/5.0026203.

[6] R. Pohlman, K. Heisler, M. Cichos, Powdering aluminium and aluminium alloys by ultrasound, Ultrasonics 12 (1974) 11–15, https://doi.org/10.1016/0041-624x(74)90080-8.

[7] Z. Wang, Fabrication of Al and Al-Si alloy microspheres by ultrasonic irradiating the molten salt-aluminum immiscible system, Ultrason. Sonochem. 50 (2019) 373–376, https://doi.org/10.1016/j.ultsonch.2018.09.039.

[8] Ł. Żrodowski, R. Wróblewski, T. Choma, B. Morończyk, M. Ostrysz, M. Leonowicz, W. Łacisz, P. Błyskun, J.S. Wróbel, G. Cieślak, B. Wysocki, C. Żrodowski, K. Pomian, Novel cold crucible ultrasonic atomization powder production method for 3D printing, Materials 14 (2021) 2541, https://doi.org/10.3390/ma14102541.

[9] P. Kustron, M. Korzeniowski, A. Sajbura, T. Piwowarczyk, P. Kaczynski, P. Sokolowski, Development of high-power ultrasonic system dedicated to metal powder atomization, Appl. Sci. 13 (2023) 8984, https://doi.org/10.3390/app13158984.

[10] Y. Zhang, S. Yuan, L. Wang, Investigation of capillary wave, cavitation and droplet diameter distribution during ultrasonic atomization, Exp. Therm. Fluid Sci. 120 (2021) 110219, https://doi.org/10.1016/j.expthermflusci.2020.110219.

[11] H. Zhang, X. Zhang, X. Yi, F He, P. Niu, P. Hao, Dynamic behaviors of droplets impacting on ultrasonically vibrating surfaces, Exp. Therm. Fluid Sci. 112 (2020) 110019, https://doi.org/10.1016/j.expthermflusci.2019.110019.

[12] G. Caccioppoli, Bernard Clausen, Christian Bonjour, Pascal Pralong, Fabrication of metal powders by ultrasonic atomisation description of an atomiser based on a new ultrasonic device, Matériaux 100 (2002) 1–4.

[13] S.H. Alavi, S.P. Harimkar, Ultrasonic vibration-assisted laser atomization of stainless steel, Powder Technol. 321 (2017) 89–93, https://doi.org/10.1016/j.powtec.2017.08.007.

[14] A. Lawley, Atomization of specialty alloy powders, JOM 33 (2014) 13–18, https://doi.org/10.1007/bf03354395.

[15] B. Avvaru, M.N. Patil, P.R. Gogate, A.B. Pandit, Ultrasonic atomization: effect of liquid phase properties, Ultrasonics 44 (2006) 146–158, https://doi.org/10.1016/j.ultras.2005.09.003.

[16] F. Barreras, H. Amaveda, A. Lozano, Transient high-frequency ultrasonic water atomization, Exp. Fluids 33 (2002) 405–413, https://doi.org/10.1007/s00348-002-0456-1.

[17] M.N. Topp, Ultrasonic atomization-a photographic study of the mechanism of disintegration, J. Aerosol Sci. 4 (1973) 17–25, https://doi.org/10.1016/0021-8502(73)90113-4.

[18] K.A. Ramisetty, A.B. Pandit, P.R. Gogate, Investigations into ultrasound induced atomization, Ultrason. Sonochem. 20 (2013) 254–264, https://doi.org/10.1016/j.ultsonch.2012.05.001.

[19] P. Deepu, C. Peng, S. Moghaddam, Dynamics of ultrasonic atomization of droplets, Exp. Therm. Fluid Sci. 92 (2018) 243–247, https://doi.org/10.1016/j.expthermflusci.2017.11.021.

[20] R. Galleguillos, Acoustic cavitation detection during ultrasonic atomization process, Appl. Acoust. 192 (2022) 108716, https://doi.org/10.1016/j.apacoust.2022.108716.

[21] R.J. Lang, Ultrasonic atomization of liquids, J. Acoust. Soc. Am. 34 (1962) 6–8.

[22] A.J. James, B. Vukasinovic, M.K. Smith, A. Glezer, Vibration-induced drop atomization and bursting, J. Fluid Mech. 476 (2003) 1–28.

[23] Y. Li, A. Umemura, Threshold condition for spray formation by Faraday instability, J. Fluid Mech. 759 (2014) 73–103.

[24] Y. Li, A. Umemura, Two-dimensional numerical investigation on the dynamics of ligament formation by Faraday instability, Int. J. Multiph. Flow 60 (2014) 64–75, https://doi.org/10.1016/jijmultiphaseflow.2013.12.002.

[25] A.J. James, M.K. Smith, A. Glezer, Vibration-induced drop atomization and the numerical simulation of low-frequency single-droplet ejection, J. Fluid Mech. 476 (2003) 29–62, https://doi.org/10.1017/s0022112002002860.

[26] E.A. Neppiras, B.E. Noltingk, Cavitation produced by ultrasonics: theoretical conditions for the onset of cavitation, Proc. Phys. Soc. Sect. B 64 (1951) 1032, https://doi.org/10.1088/0370-1301/64/12/302.

[27] K. Söllner, The mechanism of the formation of fogs by ultrasonic waves, Trans. Faraday Soc. 32 (1936) 1532–1536, https://doi.org/10.1039/TF9363201532.

[28] Y.Y. Boguslavski, Physical mechanism of the acoustic atomization of a liquid, Sov. Phys. Acoust. 15 (1969) 14–21.

[29] J.M. Mir, Cavitation-induced capillary waves in ultrasonic atomization, J. Acoust. Soc. Am. 67 (1980) 201–205, https://doi.org/10.1121/1.383728.

[30] L. Rozenberg, Physical Principles of Ultrasonic Technology, Springer Science & Business Media, 2013.

[31] T. Kouda, Y. Hagiwara, An experimental study on turbulent swirling water flow with immiscible droplets, Int. J. Heat Fluid Flow 27 (2006) 611–618, https://doi.org/10.1016/j.ijheatfluidflow.2006.02.022.

[32] A.G. Chakinala, P.R. Gogate, A.E. Burgess, D.H. Bremner, Intensification of hydroxyl radical production in sonochemical reactors, Ultrason. Sonochem. 14 (2007) 509–514, https://doi.org/10.1016/j.ultsonch.2006.09.001.

[33] R. Feng, Y. Zhao, C. Zhu, T. Mason, Enhancement of ultrasonic cavitation yield by multi-frequency sonication, Ultrason. Sonochem. 9 (2002) 231–236, https://doi.org/10.1016/S1350-4177(02)00083-4.

[34] K. Mc Carogher, Z. Dong, D.S. Stephens, M.E. Leblebici, R. Mettin, S. Kuhn, Acoustic resonance and atomization for gas-liquid systems in microreactors, Ultrason. Sonochem. 75 (2021) 105611, https://doi.org/10.1016/j.ultsonch.2021.105611.

[35] D.G. Eskin, K. Al-Helal, I. Tzanakis, Application of a plate sonotrode to ultrasonic degassing of aluminum melt: acoustic measurements and feasibility study, J. Mater. Process. Technol. 222 (2015) 148–154, https://doi.org/10.1016/j.jmatprotec.2015.03.006.

[36] Y. Goto, Y. Kito, Metallic powder production from a plate arc electrode vibrated in an ultrasonic frequency, IEEJ Trans. Fundam. Mater. 112 (1992) 695–700.

[37] G.I. Eskin, D.G. Eskin, Rapid ultrasonic solidification of aluminum alloys, in: Ultrasonic Treatment of Light Alloy Melts, second ed., CRC Press, Boca Raton, Florida, USA, 2017, pp. 284–291.

[38] I. Tzanakis, G.S.B. Lebon, D.G. Eskin, K.A. Pericleous, Characterizing the cavitation development and acoustic spectrum in various liquids, Ultrason. Sonochem. 34 (2017) 651–662, https://doi.org/10.1016/j.ultsonch.2016.06.034.

[39] L. Zrodowski, Ultrasound System for Metal and their Alloys Processing and Method of Liquid Metals Processing, WO2022034517A1, 2022. https://worldwide.espacenet.com/patent/search/family/078000738/publication/WO2022034517A1?q=pn%3DWO2022034517A1 (Accessed January 9, 2024).

[40] S. Kooij, A. Astefanei, G.L. Corthals, D. Bonn, Size distributions of droplets produced by ultrasonic nebulizers, Sci. Rep. 9 (1) (2019) 8, https://doi.org/10.1038/s41598-019-42599-8.

[41] D.J. Collins, O. Manor, A. Winkler, H. Schmidt, J.R. Friend, L.Y. Yeo, Atomization off thin water films generated by high-frequency substrate wave vibrations, Phys. Rev. E Stat. Nonlinear Soft Matter Phys. 86 (2012) 056312, https://doi.org/10.1103/PhysRevE.86.056312.

[42] E. Nazarzadeh, R. Wilson, X. King, J. Reboud, M. Tassieri, J.M. Coopera, Confinement of surface waves at the air-water interface to control aerosol size and dispersity, Phys. Fluids 29 (2017) 112105, https://doi.org/10.1063/1.4993793/105271.

[43] I. Tzanakis, D.G. Eskin, A. Georgoulas, D.K. Fytanidis, Incubation pit analysis and calculation of the hydrodynamic impact pressure from the implosion of an acoustic cavitation bubble, Ultrason. Sonochem. 21 (2014) 866–878, https://doi.org/10.1016/j.ultsonch.2013.10.003.

[44] J.A. Morton, M. Khavari, L. Qin, B.M. Maciejewska, A.V. Tyurnina, N. Grobert, D.G. Eskin, J. Mi, K. Porfyrakis, P. Prentice, I. Tzanakis, New insights into sono-exfoliation mechanisms of graphite: in situ high-speed imaging studies and acoustic measurements, Mater. Today 49 (2021) 10–22, https://doi.org/10.1016/j.mattod.2021.05.005.

[45] C.L. Goodridge, H.G.E. Hentschel, D.P. Lathrop, Breaking Faraday waves: critical slowing of droplet ejection rates, Phys. Rev. Lett. 82 (1999) 3062, https://doi.org/10.1103/PhysRevLett.82.3062.

[46] B. Vukasinovic, M.K. Smith, A. Glezer, Spray characterization during vibration-induced drop atomization, Phys. Fluids 16 (2004) 306–316, https://doi.org/10.1063/1.1632907.

[47] Y. Zhang, S. Yuan, Y. Gao, Spatial distribution and transient evolution of sub-droplet velocity and size in ultrasonic atomization, Exp. Therm. Fluid Sci. 140 (2023) 110761, https://doi.org/10.1016/j.expthermflusci.2022.110761.

[48] L. Yusuf, M.D. Symes, P. Prentice, Characterising the cavitation activity generated by an ultrasonic horn at varying tip-vibration amplitudes, Ultrason. Sonochem. 70 (2021) 105273, https://doi.org/10.1016/j.ultsonch.2020.105273.

[49] R.N. Golykh, V.A. Nesterov, A.V. Shalunova, E.V. Ilchenko, Theoretical study of the interaction of cavitation bubbles with the interface "liquid-gas" determining optimum modes of ultrasonic effect to increase the surface of the phase contact, Am. J. Eng. Res. (2014) 139–149.

[50] Y. Zhang, S. Yuan, Phase, pressure and velocity evolution and atomization characteristics of multiple Faraday waves in ultrasonic atomization: experiments and simulations, Int. J. Multiph. Flow 156 (2022) 104223, https://doi.org/10.1016/j.ijmultiphaseflow.2022.104223.

[51] S. Yuan, Y. Zhang, Y. Gao, Faraday wave instability characteristics of a single droplet in ultrasonic atomization and the sub-droplet generation mechanism, Exp. Therm. Fluid Sci. 134 (2022) 110618, https://doi.org/10.1016/j.expthermfluisci.2022.110618.

[52] V.A. Aleksandrov, S.P. Kopysov, L.Y. Tonkov, Jet formation at interaction of a vibrating plate with liquid, IOP Conf. Ser. Mater. Sci. Eng. 208 (2017) 012001, https://doi.org/10.1088/1757-899x/208/1/012001.

[53] V.A. Aleksandrov, Vibrational spraying of liquid by a thin rod, Tech. Phys. Lett. 34 (2008) 100–102, https://doi.org/10.1134/s1063785008020041/metrics.

[54] R. Mettin, I. Akhatov, U. Parlitz, C.D. Ohl, W. Lauterborn, Bjerknes forces between small cavitation bubbles in a strong acoustic field, Phys. Rev. E 56 (1997) 2924, https://doi.org/10.1103/PhysRevE.56.2924.

[55] N.A. Pelekasis, A. Gaki, A. Doinikov, J.A. Tsamopoulos, Secondary Bjerknes forces between two bubbles and the phenomenon of acoustic streamers, J. Fluid Mech. 500 (2004) 313–347, https://doi.org/10.1017/S0022112003007365.

[56] X. Wang, Z. Ning, M. Lv, J. Yao, C. Sun, The secondary bjerknes force between two bubbles in ultrasonic field, J. Phys. Soc. Jpn. 91 (2021), https://doi.org/10.7566/JPSJ.91.014401.

[57] M. Khavari, A. Priyadarshi, J. Morton, K. Porfyrakis, K. Pericleous, D. Eskin, I. Tzanakis, Cavitation-induced shock wave behaviour in different liquids, Ultrason. Sonochem. 94 (2023) 106328, https://doi.org/10.1016/j.ultsonch.2023.106328.

[58] Lord Rayleigh, The theory of sound, Nature 58 (1898) 121–122, https://doi.org/10.1038/058121a0.

[59] A. Qi, L.Y. Yeo, J.R. Friend, Interfacial destabilization and atomization driven by surface acoustic waves, Phys. Fluids 20 (2008), https://doi.org/10.1063/1.2953537/256596.

[60] C. Dumouchel, D. Sindayihebura, L. Bolle, Application of the maximum entropy formalism on sprays produced by ultrasonic atomizers, Part. Part. Syst. Charact. 20 (2003) 150–161, https://doi.org/10.1002/ppsc.200390012.

[61] S. Douady, Experimental study of the Faraday instability, J. Fluid Mech. 221 (1990) 383–409, https://doi.org/10.1017/S0022112090003603.

[62] The stability of the plane free surface of a liquid in vertical periodic motion, Proc. R. Soc. London. Ser. A. Math. Phys. Sci., 225 (1954), pp. 505–515. https://doi.org/10.1098/RSPA.1954.0218.

[63] E. Mahravan, H. Naderan, E. Damangir, Frequency and wavelength prediction of ultrasonic induced liquid surface waves, Ultrasonics 72 (2016) 184–190, https://doi.org/10.1016/j.ultras.2016.08.002.

[64] A. Žnidarčič, R. Mettin, C. Cairós, M. Dular, Attached cavitation at a small diameter ultrasonic horn tip, Phys. Fluids 26 (2014) 023304, https://doi.org/10.1063/1.4866270.

[65] A. Priyadarshi, M. Khavari, T. Subroto, M. Conte, P. Prentice, K. Pericleous, D. Eskin, J. Durodola, I. Tzanakis, On the governing fragmentation mechanism of primary intermetallics by induced cavitation, Ultrason. Sonochem. 70 (2021) 105260, https://doi.org/10.1016/j.ultsonch.2020.105260.

[66] M. Khavari, A. Priyadarshi, A. Hurrell, K. Pericleous, D. Eskin, I. Tzanakis, Characterization of shock waves in power ultrasound, J. Fluid Mech. 915 (2021) R3, https://doi.org/10.1017/jfm.2021.186.

[67] Y. Renardy, S. Popinet, L. Duchemin, M. Renardy, S. Zaleski, C. Josserand, M. A. Drumright-Clarke, D. Richard, C. Clanet, D. Quéré, Pyramidal and toroidal water drops after impact on a solid surface, J. Fluid Mech. 484 (2003) 69–83, https://doi.org/10.1017/S0022112003004142.

[68] K. Yasuda, Y. Bando, S. Yamaguchi, M. Nakamura, A. Oda, Y. Kawase, Analysis of concentration characteristics in ultrasonic atomization by droplet diameter distribution, Ultrason. Sonochem. 12 (2005) 37–41, https://doi.org/10.1016/j.ultsonch.2004.05.008.

[69] J.H. Tan, W.L.E. Wong, K.W. Dalgarno, An overview of powder granulometry on feedstock and part performance in the selective laser melting process, Addit. Manuf. 18 (2017) 228–255, https://doi.org/10.1016/J.ADDMA.2017.10.011.

[70] S. Yuan, Y. Zhang, Y. Gao, Faraday instability of a liquid layer in ultrasonic atomization, Phys. Rev. Fluids 7 (2022) 033902, https://doi.org/10.1103/PhysRevFluids.7.033902.

[71] D. Šarkovic, V. Babovic, On the statistics of ultrasonically produced water droplets, Z. Naturforsch. Sect. A J. Phys. Sci. 60 (2005) 489–493, https://doi.org/10.1515/zna-2005-0704.

[72] P. Moghimian, T. Poirié, M. Habibnejad-Korayem, J.A. Zavala, J. Kroeger, F. Marion, F. Larouche, Metal powders in additive manufacturing: a review on reusability and recyclability of common titanium, nickel and aluminum alloys, Addit. Manuf. 43 (2021) 102017, https://doi.org/10.1016/j.addma.2021.102017.

[73] T. Fedina, Laser beam-material interaction in powder bed fusion, Luleå Univ. Technol. (2021).

[74] R. Rajan, A.B. Pandit, Correlations to predict droplet size in ultrasonic atomisation, Ultrasonics 39 (2001) 235–255, https://doi.org/10.1016/S0041-624X(01)00054-3.